Pore Wetting Mitigation in Membrane Distillation: A Mechanistic Model for Water Flow in Janus Membranes and a 3D Morphology-Based Model for Liquid Entry Pressure

By

Alireza Chamani

Thesis submitted to the University of Ottawa in partial fulfillment
of the requirements for the

Master of Applied Science in Chemical Engineering

uOttawa

Department of Chemical and Biological Engineering
University of Ottawa

Abstract

Water scarcity is a rapidly growing concern worldwide. Since 97% of Earth's water is seawater, there is great potential to tackle this challenge by removing salts from saline water to produce freshwater, a process that is called desalination. Among desalination methods, membrane-based processes have gained attention due to their efficiency in separating salt from water.

Reverse Osmosis (RO) process is the state-of-the-art desalination technology, but it is incapable of desalting high salinity brines. Membrane Distillation (MD) is a promising solution for high salinity brines. However, it has a main challenge in pore wetting, which happens when liquid water passes through the pores. To this end, Janus membranes have drawn attention as their unique feature of having one side hydrophobic and the other hydrophilic and have been experimentally demonstrated to enhance pore wetting in MD. Furthermore, the liquid entrance pressure (LEP) is a key feature that determines the pore wetting prevention in conventional MD membranes.

In this research, we first developed a model to simulate the directional transport of liquid water in the pores of the Janus membrane by calculating the surface energy change in association with the movement of water in a pore of a Janus membrane. It was demonstrated that when the hydrophilic side of the Janus membrane was designated as the feed side, the critical pressure to be overcome for liquid water to penetrate the pores of the hydrophobic layer would increase and therefore help prevent pore wetting. On the other hand, spontaneous liquid water flow will take place when the membrane is inverted. These simulation results unambiguously revealed the mechanism underlying the enhancement of pore wetting prevention by Janus membranes, i.e., the combination of the expulsion by the hydrophobic layer and the pulling by the hydrophilic layer to liquid water at the interface.

Furthermore, we developed a 3D morphology-based model capable of analyzing 3D images of porous hydrophobic membranes to estimate LEP rapidly without requiring idealizations. The developed model was validated using the 3D image of a commercial membrane, PT20 from Gore Inc., and the corresponding experimental LEP reported in the previously published literatures. Using this model, we further investigated the effects of membrane morphological features including the max pore radius, mean pore radius, and throat radius, on LEP.

Résumé

La pénurie d'eau est une préoccupation croissante dans le monde entier. Étant donné que 97 % de l'eau de la Terre est de l'eau de mer, il existe un grand potentiel pour relever ce défi en éliminant les sels de l'eau salée pour produire de l'eau douce, un processus appelé dessalement. Parmi les méthodes de dessalement, les procédés à base de membranes ont attiré l'attention en raison de leur efficacité à séparer le sel de l'eau.

Le procédé d'osmose inverse (RO) est la technologie de dessalement de pointe, mais il est incapable de dessaler les saumures à haute salinité. La distillation membranaire (MD) est une solution prometteuse pour les saumures à haute salinité. Cependant, elle présente un défi majeur dans le mouillage des pores, qui se produit lorsque l'eau liquide traverse les pores. À cette fin, les membranes Janus ont attiré l'attention en raison de leur caractéristique unique d'avoir un côté hydrophobe et l'autre hydrophile et il a été démontré expérimentalement qu'elles améliorent le mouillage des pores dans la MD. De plus, la pression d'entrée du liquide (LEP) est une caractéristique clé qui détermine la prévention du mouillage des pores dans les membranes MD conventionnelles.

Dans cette recherche, nous avons d'abord développé un modèle pour simuler le transport directionnel de l'eau liquide dans les pores de la membrane Janus en calculant le changement d'énergie de surface en association avec le mouvement de l'eau dans un pore d'une membrane Janus. Il a été démontré que lorsque le côté hydrophile de la membrane Janus était désigné comme côté d'alimentation, la pression critique à surmonter pour que l'eau liquide pénètre dans les pores de la couche hydrophobe augmenterait et aiderait donc à empêcher le mouillage des pores. D'autre part, un écoulement spontané de l'eau liquide aura lieu lorsque la membrane est inversée. Ces résultats de simulation ont révélé sans ambiguïté le mécanisme sous-jacent à l'amélioration de la

prévention du mouillage des pores par les membranes Janus, c'est-à-dire la combinaison de l'expulsion par la couche hydrophobe et de l'attraction par la couche hydrophile vers l'eau liquide à l'interface.

De plus, nous avons développé un modèle basé sur la morphologie 3D capable d'analyser des images 3D de membranes hydrophobes poreuses pour estimer rapidement le LEP sans nécessiter d'idéalisations. Le modèle développé a été validé à l'aide de l'image 3D d'une membrane commerciale, PT20 de Gore Inc., et du LEP expérimental correspondant rapporté dans les publications précédentes. À l'aide de ce modèle, nous avons étudié plus en détail les effets des caractéristiques morphologiques de la membrane, notamment le rayon maximal des pores, le rayon moyen des pores et le rayon de la gorge, sur le LEP.

Dedication

This thesis is dedicated to my parents, Shahnaz and Mahdi, for their love, support, and guidance and to my family and friends, who helped during this journey.

Statement of contributions

I declare that I am the sole author of this thesis and that I performed the model development and validation.

Dr. Arash Rabbani from the University of Leeds, UK, provided guidance throughout the liquid entry pressure estimation project.

My thesis supervisors, Prof. Christopher Lan and Prof. Takeshi Matsuura at the Department of Chemical and Biological Engineering, University of Ottawa, offered scientific supervision, invaluable advice, and editorial feedback on the written work and helped me with the model development. Additionally, Dr. Dipak Rana provided advice on the thesis writing process.

Acknowledgement

I would like to express my heartfelt gratitude to my supervisors, Prof. Christopher Lan and Prof. Takeshi Matsuura, for their exceptional mentorship, continuous guidance, and thoughtful contributions throughout my research. I am sincerely thankful to Dr. Arash Rabbani from the School of Computing at the University of Leeds for his advice and assistance. I also want to give special thanks to Dr. Dipak Rana, whose support has been incredibly helpful. I am also grateful to the University of Ottawa for awarding me the Merit Scholarship. Lastly, I would like to acknowledge the invaluable support of my family, friends and colleagues who accompanied me throughout this journey.

Table of contents

List of figures

List of tables

Abbreviation

CA	Cellulose Acetate
CFD	Computational Fluid Dynamics
cSAXS	coherent Small-Angle X-ray Scattering
FO	Forward Osmosis
LEP	Liquid Entry Pressure
MD	Membrane Distillation
MF	Microfiltration
NF	Nanofiltration
PAN	Polyacrylonitrile
PE	Polyethylene
PES	Polyether Sulfone
PPO	Polyphenylene Oxide
PP	Polypropylene
PU	Polyurethane
PV	Pervaporation
PVA	Polyvinyl Alcohol
PVDF	Polyvinylidene Fluoride
PSt	Polystyrene
PTFE	Polytetrafluoroethylene
RO	Reverse Osmosis
SS	Stainless Steel
UF	Ultrafiltration
VOF	Volume of Fluid

Symbols

θ	Contact angle (°)
φ	Local geometrical angle (°)
α	Effective contact angle (°)
r	Radius (m)
R	Fiber radius (m)
L	Length of the pore (m)
d_0	Edge-to-edge distance in fibers (m)
ν	Flow rate (m^3/s)
R	Ideal gas constant (m^3.Pa/k.mol)
T	Temperature (°C)
ΔP	Pressure difference (Pa)
p_f	Feed pressure (Pa)
p_p	Permeate pressure (Pa)
p_c	Critical pressure (Pa)
Π	Osmotic pressure (Pa)
c	Concentration (mol/L)
σ_{sg}	Surface tension of solid/gas (N/m)
σ_{sl}	Surface tension of solid/liquid (N/m)
σ	Surface tension of liquid/gas (N/m)
γ	Surface tension (N/m)
η	Viscosity ($N.s/m^2$)
B	Franken pore geometry coefficient (-)
i	The van't Hoff index (-)

Chapter 1: Introduction

Water is fundamental to life on Earth, playing an important role in human life [1]. The excessive use of freshwater threatens food security and human well-being in most of the world. The challenge of keeping water usage at sustainable levels is going to be even more difficult in the upcoming years, mainly because of increasing population pressure, changing water consumption behaviour, and climate change [2]. Even Canada suffers from drought in some parts as can be seen in Fig. 1-1, based on Agriculture and Agri-Food Canada [3].

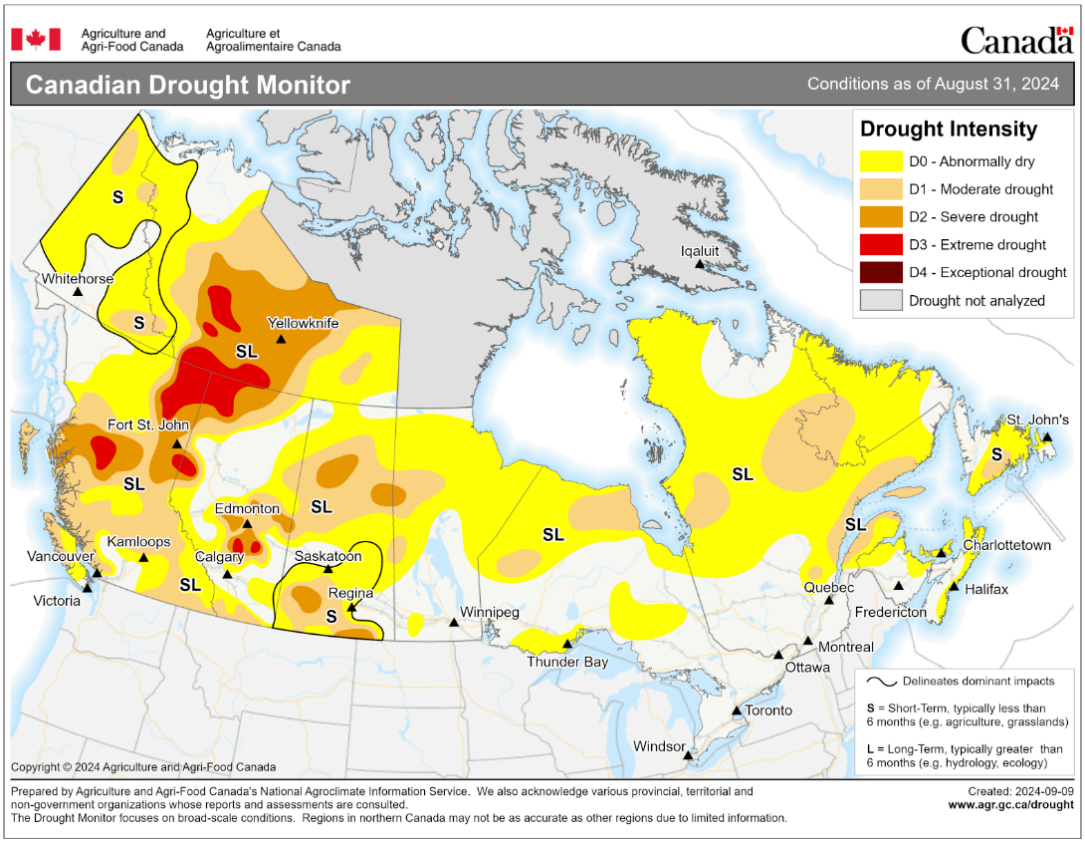

Fig. 1-1. The map of the extent and severity of drought conditions across Canada, prepared by Agriculture and Agri-Food Canada [3].

The surface of Earth is 71% water, and 97% of this water is seawater [4]. Since seawater is not suitable for human consumption, the world population relies on only 3% of available freshwater. Only 0.06% of these freshwater resources are easily accessible, as most of them are polar ice caps, glaciers, groundwater, and swamps [5].

Due to the limited freshwater resources, desalination, the process of treating saline water to produce fresh water, has been a promising solution for water supply in many countries which suffer from limited access to fresh water [6].

A known and popular method in desalination is membrane-based desalination. These membrane technologies include forward osmosis (FO), reverse osmosis (RO), membrane distillation (MD), pervaporation (PV), microfiltration (MF), ultrafiltration (UF), and nanofiltration (NF) [7]. One of the most important characterization parameters in membranes is hydrophobicity, high hydrophobicity is associated with a high water contact angle [8]. Membranes, based on their type and the process in which they are used, are hydrophilic or hydrophobic. For instance, in MD, a highly hydrophobic membrane is desired to prevent the liquid from passing through the membrane [9]. MD is a non-isothermal membrane separation process [10] and consumes thermal energy to provide a vapor phase of volatile molecules from the feed stream, and then permeated vapor condenses on the cooler side. When liquid enters the pores instead of vapour, pore wetting occurs which reduces flux, permeate quality, and even membrane lifetime, so this is the reason that hydrophobic membranes are used in MD. In contrast, in NF, and RO, a hydrophilic membrane is preferred to allow liquid to pass [11]. Recently, a new kind of membrane was introduced which has different properties on each side, called the Janus membrane. The name of these membranes comes from “Janus” which is the two-faced god in ancient Roman mythology [12]. A popular type of Janus membrane is the one with different hydrophobicity on each side (as can be seen in Fig. 1-

2). Janus membranes could potentially be used in a wide range of applications, mostly in processes such as oil-water separation, MD, solar evaporation, electrodialysis, NF, and FO [13]. As an example, Janus membrane is helpful in solar-interfacial desalination; the bottom of the Janus membrane is made with hydrophilic materials like polyacrylonitrile (PAN) which function as capillary pumps to ensure a continuous water supply, the top surface is made of hydrophobic materials like polyvinylidene fluoride (PVDF) which offers self-floating properties and enhances solar-to-vapor conversion efficiency [14]. We developed a model for fluid flow in the pores of Janus membranes. In recent years, Janus membranes, or "two-faced" membranes have shown promising potential in many applications, especially desalination [16]. While numerous studies have focused on the fabrication, characterization, and experimental performance evaluation of Janus membranes, there remains a gap in understanding their transport mechanisms. Our work addresses this gap by developing a fundamental model, contributing to a deeper understanding of these membranes' behavior.

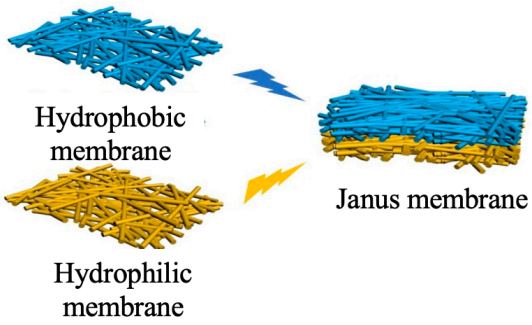

Fig. 1-2. An example of a Janus membrane with different contact angles on each side [15].

On the other hand, the liquid entrance pressure of water (LEP) is a key feature that controls the pore wetting process in conventional MD membranes and plays a significant role in Janus membranes. Understanding how different membrane features affecting LEP is therefore of

paramount importance in developing effective pore wetting mitigation strategies. However, existing models for LEP, e.g., Young Laplace, Franken, Kim, and Servi models [9,18–20], have typically been developed for ideal pores, such as torus and cylindrical shapes. Whereas membrane pores are highly complicated and consist of many interconnected pores with different pore sizes. To address the complexity of membrane pores, one solution is to use computational fluid dynamics (CFD) [21]. However, applying CFD at the pore scale with this level of membrane structure complexity is very time-consuming and may take days, for example, using GeoDict software [22]. Adding to that, it requires supercomputers, which are not typically accessible. Therefore, we developed a 3D morphology-based model that can estimate LEP very quickly without employing CFD tools.

1.1. Thesis objectives

The main goal of this research is to develop pore wetting mitigation strategies for membrane distillation from two different aspects.

i) Developing a model for water flow inside the pores and across the hydrophobic/hydrophilic interface in Janus membranes to understand the mechanisms underlying their enhanced pore wetting resistance.

ii) Developing a 3D morphology-based model for LEP estimation, and thereby enhancing our understanding of the key factors affecting the LEP of a membrane, which is a key factor in pore wetting resistance in MD membranes and then using the model to identify the key morphological features dictating LEP.

1.2. Thesis outlines

This thesis includes four chapters and is presented in the form of a series of manuscripts. Chapter 1 is the Introduction. Chapter 2 includes model development for fluid movement within the pores of Janus membranes, with one layer hydrophobic and the other hydrophilic. In Chapter 3, a 3D morphology-based machine learning model is developed that uses the parameters derived from a 3D image of a hydrophobic membrane to calculate LEP. Finally, Chapter 4 presents the conclusions of the thesis and discusses some suggestions for further studies.

1.3. References

[1] Shiklomanov IA. Appraisal and assessment of world water resources. Water Int 2000;25:11–32. https://doi.org/10.1080/02508060008686794.

[2] Kummu M, Guillaume JHA, de Moel H, Eisner S, Flörke M, Porkka M, et al. The world's road to water scarcity: shortage and stress in the 20th century and pathways towards sustainability. Sci Rep 2016;6:38495. https://doi.org/10.1038/srep38495.

[3] Canadian Drought Monitor. https://agriculture.canada.ca/en/agricultural-production/weather/canadian-drought-monitor.

[4] Kalogirou S. Seawater desalination using renewable energy sources. Prog Energy Combust Sci 2005;31:242–81. https://doi.org/10.1016/j.pecs.2005.03.001.

[5] Musie W, Gonfa G. Fresh water resource, scarcity, water salinity challenges and possible remedies: A review. Heliyon 2023;9:e18685. https://doi.org/10.1016/j.heliyon.2023.e18685.

[6] Elsaid K, Kamil M, Sayed ET, Abdelkareem MA, Wilberforce T, Olabi A. Environmental impact of desalination technologies: A review. Science of The Total Environment 2020;748:141528. https://doi.org/10.1016/j.scitotenv.2020.141528.

[7] Aliyu UM, Rathilal S, Isa YM. Membrane desalination technologies in water treatment: A review. Water Pract Technol 2018;13:738–52. https://doi.org/10.2166/wpt.2018.084.

[8] Law K-Y. Water–surface interactions and definitions for hydrophilicity, hydrophobicity and superhydrophobicity. Pure and Applied Chemistry 2015;87:759–65. https://doi.org/10.1515/pac-2014-1206.

[9] Servi AT, Kharraz J, Klee D, Notarangelo K, Eyob B, Guillen-Burrieza E, et al. A systematic study of the impact of hydrophobicity on the wetting of MD membranes. J Memb Sci 2016;520:850–9. https://doi.org/10.1016/j.memsci.2016.08.021.

[10] Khayet M. Membranes and theoretical modeling of membrane distillation: A review. Adv Colloid Interface Sci 2011;164:56–88. https://doi.org/10.1016/j.cis.2010.09.005.

[11] Akin O, Temelli F. Probing the hydrophobicity of commercial reverse osmosis membranes produced by interfacial polymerization using contact angle, XPS, FTIR, FE-SEM and AFM. Desalination 2011;278:387–96. https://doi.org/10.1016/j.desal.2011.05.053.

[12] Yang H, Xie Y, Hou J, Cheetham AK, Chen V, Darling SB. Janus Membranes: Creating Asymmetry for Energy Efficiency. Advanced Materials 2018;30. https://doi.org/10.1002/adma.201801495.

[13] Meng L, Shi W, Li Y, Li X, Tong X, Wang Z. Janus membranes at the water-energy nexus: A critical review. Adv Colloid Interface Sci 2023;318:102937. https://doi.org/10.1016/j.cis.2023.102937.

[14] Guo Y, Wan Y, Zhang Y, Pan G, Wang J, Yu H, et al. Janus porous membranes with asymmetric wettability and self-floating properties for solar desalination. Journal of Polymer Research 2023;30:37. https://doi.org/10.1007/s10965-022-03392-w.

[15] Tang S, Pi H, Zhang Y, Wu J, Zhang X. Novel Janus fibrous membranes with enhanced directional water vapor transmission. Applied Sciences 2019;9:3302. https://doi.org/10.3390/app9163302.

[16] Afsari M, Shon HK, Tijing LD. Janus membranes for membrane distillation: Recent advances and challenges. Adv Colloid Interface Sci 2021;289:102362. https://doi.org/10.1016/j.cis.2021.102362.

[17] Rácz G, Kerker S, Kovács Z, Vatai G, Ebrahimi M, Czermak P. Theoretical and experimental approaches of liquid entry pressure determination in membrane distillation processes. Periodica Polytechnica Chemical Engineering 2014;58:81–91. https://doi.org/10.3311/PPch.2179.

[18] Chamani H, Yazgan-Birgi P, Matsuura T, Rana D, Hassan Ali MI, Arafat HA, et al. CFD-based genetic programming model for liquid entry pressure estimation of hydrophobic membranes. Desalination 2020;476:114231. https://doi.org/10.1016/j.desal.2019.114231.

[19] Franken ACM, Nolten JAM, Mulder MHV, Bargeman D, Smolders CA. Wetting criteria for the applicability of membrane distillation. J Memb Sci 1987;33:315–28. https://doi.org/10.1016/S0376-7388(00)80288-4.

[20] Guillen-Burrieza E, Servi A, Lalia BS, Arafat HA. Membrane structure and surface morphology impact on the wetting of MD membranes. J Memb Sci 2015;483:94–103. https://doi.org/10.1016/j.memsci.2015.02.024.

[21] Jäger T, Mokos A, Prasianakis NI, Leyer S. Pore-level multiphase simulations of realistic distillation membranes for water desalination. Membranes (Basel) 2022;12:1112. https://doi.org/10.3390/membranes12111112.

[22] Calo VM, Di Nicolò E, Iliev O, Lakdawala Z, Leonard KH, Printsypar G. Simulation of osmotic and reactive effects in membranes with resolved microstructure. Proceedings of the FILTECH. 2015;2015.

Chapter 2: Modeling of water transport in Janus membrane

Chapter 2 contains an adapted version of the manuscript that is under review for publication in the Desalination journal.

Directional water transport of Janus membrane: a theoretical approach

Alireza Chamani, Dipak Rana, Takeshi Matsuura, Christopher Lan

Department of Chemical and Biological Engineering, University of Ottawa,

Ottawa, Ontario K1N 6N5, Canada

2.1. Abstract

Membranes with asymmetric properties on different sides are called Janus membranes. A typical example is the membrane with the transition from the hydrophilic feed side to the hydrophobic permeate side or vice versa. Janus membranes exhibit unique transport characteristics, such as directional transport of solvents or solutes. There are many reports on Janus membranes for various applications and the number has been increasing recently. However, most of them are experimental with only few works on the transport theory. In this work, an innovative attempt is made to explain the directional transport of the Janus membrane by the surface energy change that is caused by the movement of water in a pore in which the contact angle changes from one side to the other. This approach, based on the Young equation, is simple and allows to compute the water flux when it takes place. The model also shows that the Janus membrane with hydrophilic/hydrophobic configuration can greatly improve resistance to pore wetting in membrane distillation.

2.2. Introduction

Membranes with asymmetric properties on different sides are called Janus membranes, named after the god with two faces of the ancient Roman mythology [1]. A typical example is the membrane transitioning from hydrophilic property of the feed side to hydrophobic property on the permeate side or vice versa. Unlike conventional membranes, Janus membranes exhibit unique transport characteristics, such as directional transport of solvents or solutes and switchable permeation. An excellent review paper was written recently [2].

There are a number of applications of Janus membranes. Typically, they are applications in oil/water separation, membrane distillation, solar evaporation, electrodialysis, nanofiltration, and forward osmosis [2].

There are also many reports on Janus membranes as can be seen in Table 1-1 and the number has increased recently.

Table 2-1. Reports worked on the applications of Janus membranes.

Janus membrane applications	Papers	References
Membrane distillation	Development of a dual-layered PVDF-HFP/Cellulose membrane with dual wettability for desalination of oily wastewater	Makanjuola et al. [3]
	Hierarchical Janus membrane with superior fouling and wetting resistance for efficient water recovery from challenging wastewater via membrane distillation	Zhao et al. [4]
	Novel Janus composite hollow fiber membrane-based direct contact membrane distillation (DCMD) process for produced water desalination	Zou et al. [5]
	Carbon nanotube based Janus composite membrane of oil fouling resistance for direct contact membrane distillation	Han et al. [6]
Oil/water separation	Janus membranes with asymmetric wettability applied in oil/water emulsion separations	Zhang et al. [7]
	Bioinspired oil-water separation approaches for oil spill clean-up and water purification	Bhushan [8]
	Simply realizing durable dual Janus superwettable membranes integrating underwater low-oil-adhesive with super-water-repellent surfaces for controlled oil–water permeation	Lin et al. [9]
	Hollow fiber membranes with Janus surfaces for continuous deemulsification and separation of oil-in-water emulsions	Li et al. [10]
	Development of Janus membrane with controllable asymmetric wettability for highly-efficient oil/water emulsions separation	Lin et al. [11]
	Directional water-transfer through fabrics induced by asymmetric wettability	Wang et al. [12]
	Capillary effect in Janus electrospun nanofiber membrane for oil/water emulsion separation	Liang et al. [13]
	Design of a Janus F-TiO2@PPS porous membrane with asymmetric wettability for switchable oil/water separation	Yang et al. [14]
	Interpenetrating Janus membrane for high rectification ratio liquid unidirectional penetration	Hou et al. [15]

Despite many experimental works, most of them are for membrane fabrication, characterization and performance evaluation, and there are only few works on the modelling of transport in Janus

membranes. One of the exceptions is Tian et al.'s work in which they have explained by a detailed model calculation why directional transport occurs in the membrane with a contact angle gradient [16]. They modeled the fiber bundles of the Janus membrane by an array of cylinders of radius r arranged parallel to each other with an edge-to-edge distance of d_o (Fig. 2-1). They also assumed that the advancing water contact angle $\theta(\varphi)$ is a function of φ, where φ is a local geometrical angle as shown in Fig. 2-1.

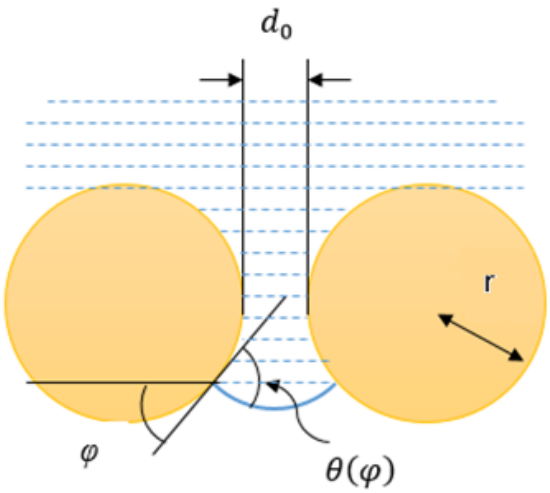

Fig. 2-1. Schematic diagram of parallel fiber bundles.

Then, Δp that is the pressure required for water to pass through the position φ is calculated by:

$$\Delta p = \frac{\gamma}{r} \times \frac{\sin[\theta(\varphi)-\varphi]}{k+1-\sin\varphi} \tag{2-1}$$

where γ is surface tension of water and $k = \frac{d_0}{2r}$.

Note that φ is equal to π at the top of the cylinder and 0 at the bottom. For an extreme case of $\theta = \varphi$, which means that the contact angle of the membrane changes from π (hydrophobic) of the top

to 0 of the hydrophilic bottom, $\Delta p = 0$ from equation (2-1), and water flows freely through the membrane. However, when the membrane is flipped (i.e. membrane is hydrophilic at the top and hydrophobic at the bottom), the contact angle is given by $\theta = \pi - \varphi$ and equation (2-1) becomes,

$$\Delta p = \frac{\gamma}{r} \times \frac{\sin[\pi - 2\varphi]}{k + 1 - \sin\varphi} \tag{2-2}$$

Equation (2-2) shows a maximum of Δp at a $\varphi < \frac{\pi}{2}$. This maximum value of Δp was called critical breakthrough pressure p_c, and Tian et al. plotted p_c as a function of *k.*

Briefly, there is free water flow when the top of the membrane is hydrophobic and the bottom is hydrophilic, but a pressure higher than p_c is required to let water flow when the membrane is flipped. Thus, Tian et al. successfully explained the directional flow of the Janus membrane.

It should be noted that Tian's model requires the presence of water/air interface and also enlarging of the water channel width toward the bottom of the membrane, called re-entrant structure.

In this work, a new attempt is made to explain the directional transport of the Janus membrane by the surface energy change that is caused by the movement of water in a pore in which the contact angle changes from one side to the other.

This new approach, based on the Young equation (which will be shown in section 2.3), is very simple and does not need the re-entrant structure, and necessarily changing radius in the pores due to the fibrous structure of membrane considered in Tian's model. The developed model equations allow to compute the water flux when the flow takes place. Moreover, the model explains why the flow rate increases when a hydrophobic layer is coated on top of a hydrophilic substrate membrane, as it was reported by Zoka et al. [17] and Dobosz et al. [18]. Uniquely, the model does not require the presence of air/water interfaces in the pore for explanation.

It is important to mention that this study predicts the presence of the hysteresis loop in the flow rate of Janus membranes and the effect of the order of magnitude larger surface energy of the metal on the critical pressure and flow rate of the Janus membrane. These phenomena have not been previously documented in the literature.

2.3. Theory

In the following model development, an assumption is made that water is in a cylindrical pore on the left side with a radius r_1 and a cylindrical pore on the right side with a radius r_2. The left side is made of a material with a contact angle of θ_1 and the right side with θ_2. It is also assumed that water moves from the left pore by a distance of dx to the right pore and the driving force for this movement is supplied by the surface energy change caused by the movement of water. The surface was assumed to be smooth and there is no roughness.

To develop our model, the following three cases are considered:

Case a) The water in the pore has a meniscus at both ends. The purpose of this case is to justify this approach by deriving the well-known equation for capillary forces.

Case b) The water in the left pore is connected to a water reservoir and in the right pore there is a meniscus. The purpose of this case is to evaluate the critical pressure that is necessary to start the water flow from left to right when the left pore is hydrophilic and the right pore hydrophobic.

Case c) The water in the left pore is connected to a water reservoir and the water in the right pore is connected to another reservoir, i.e., the pore is filled with water. The purpose of this case is to

evaluate the critical pressure that is necessary to maintain water flow from left to right after the meniscus in the right pore disappears.

In Case a), the water has a meniscus at both ends as can be seen in Fig. 2-2.

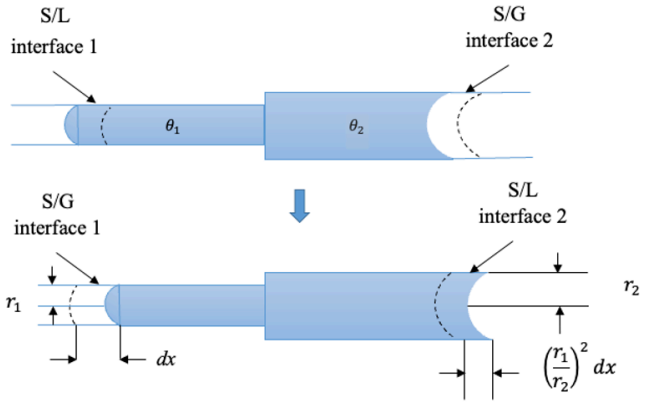

Fig. 2-2. Water in two cylindrical pores with a meniscus in each pore.

When the water in the left pore moves rightward by a distance of *dx*, the solid/liquid (s/l) contact of the area $2\pi r_1 dx$ is replaced by the solid/gas (s/g) contact. This movement causes the energy increase of $2\pi r_1 dx(\sigma_{sg,1} - \sigma_{sl,1})$, where σ_{sg} and σ_{sl} are the solid/gas and solid/liquid interfacial tension, respectively (Fig. 2-2).

Considering Young's equation,

$$\sigma_{sg,1} = \sigma_{sl,1} + \sigma \cos\theta_1 \tag{2-3}$$

the increase in surface energy is $2\pi r_1 dx\sigma \cos\theta_1$, where σ is surface tension of liquid (water).

On the other hand, on the right side, the distance of $\left(\frac{r_1}{r_2}\right)^2 dx$ moves rightward with a change of contact from solid/gas (s/g) to solid/liquid (s/l), which causes the increase of energy $2\pi r_2 \left(\frac{r_1}{r_2}\right)^2 dx(\sigma_{sl,2} - \sigma_{sg,2}) = -2\pi r_2 \left(\frac{r_1}{r_2}\right)^2 dx \cos\theta_2$

Combining both, the overall increase in the energy caused by the rightward movement of the water is $2\pi dx\sigma\left(r_1\cos\theta_1 - r_2\left(\frac{r_1}{r_2}\right)^2\cos\theta_2\right)$. Or, in terms of the decrease of the surface energy,

$-2\pi dx\sigma\left(r_1\cos\theta_1 - r_2\left(\frac{r_1}{r_2}\right)^2\cos\theta_2\right) = 2\pi dx\sigma\left(r_2\left(\frac{r_1}{r_2}\right)^2\cos\theta_2 - r_1\cos\theta_1\right)$, which is released.

Suppose the movement of the water is caused by a pressure difference Δp_a, the work required for the movement is $\pi {r_1}^2 dx\Delta p_a$, (volume of water that moves times pressure difference), which is done by the energy released by the movement of water.

Hence,

$$\pi {r_1}^2 dx\Delta p_a = 2\pi dx\sigma\left(r_2\left(\frac{r_1}{r_2}\right)^2\cos\theta_2 - r_1\cos\theta_1\right) \tag{2-4}$$

and

$$\Delta p_a = 2\sigma\left(\frac{\cos\theta_2}{r_2} - \frac{\cos\theta_1}{r_1}\right) \tag{2-5}$$

This equation is well known as the capillary force between two menisci.

Case b) shows that the water in the left pore is connected to a water reservoir and in the right pore there is a meniscus as can be seen in Fig. 2-3.

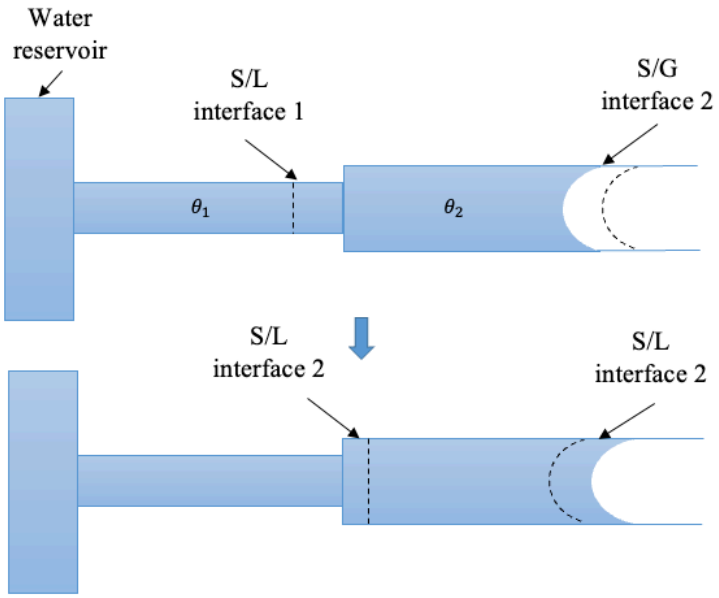

Fig. 2-3. The left pore is connected to a reservoir and the right pore is partially filled, forming a meniscus.

The water moves by a distance of *dx* from the left side with a contact angle of θ_1 to the right side with a contact angle θ_2 . Then, the change in contact is from the initial (s/l) on the left side and (s/g) on the right side to 2(s/l) on the left side (see Fig. 2-3). Thus, the increment in energy is

$$4\pi r_2 \left(\frac{r_1}{r_2}\right)^2 dx\, \sigma_{sl,2} - \left\{2\pi r_1 dx \sigma_{sl,1} + 2\pi r_2 \left(\frac{r_1}{r_2}\right)^2 dx \sigma_{sg,2}\right\}$$

Applying Young's equation and rearranging, it becomes

$$-4\pi r_2 \left(\frac{r_1}{r_2}\right)^2 dx\, \sigma\cos\theta_2 + 2\pi r_1 dx\, \sigma\cos\theta_1 + 2\pi r_2 \left(\frac{r_1}{r_2}\right)^2 dx\, \sigma_{sg,2} - 2\pi r_1 dx \sigma_{sg,1}$$

Or the decrease in energy is $\left(4\pi r_2\left(\frac{r_1}{r_2}\right)^2 dx\,\sigma\cos\theta_2 - 2\pi r_1 dx\,\sigma\cos\theta_1\right) -$

$\left(2\pi r_2\left(\frac{r_1}{r_2}\right)^2 dx\,\sigma_{sg,2} - 2\pi r_1 dx\sigma_{sg,1}\right)$

Suppose the work of $\pi {r_1}^2 dx\Delta p_b$ is done by this energy release

$$\pi {r_1}^2 dx\Delta p_b = \left(4\pi r_2\left(\frac{r_1}{r_2}\right)^2 dx\,\sigma\cos\theta_2 - 2\pi r_1 dx\,\sigma\cos\theta_1\right) - \left(2\pi r_2\left(\frac{r_1}{r_2}\right)^2 dx\,\sigma_{sg,2} - 2\pi r_1 dx\sigma_{sg,1}\right) \quad (2\text{-}6)$$

and

$$\Delta p_b = 2\sigma\left(\frac{2\cos\theta_2}{r_2} - \frac{\cos\theta_1}{r_1}\right) - 2\left(\frac{\sigma_{sg,2}}{r_2} - \frac{\sigma_{sg,1}}{r_1}\right) \quad (2\text{-}7)$$

When the pressure in the reservoir is p_f, and that at the meniscus is p_p(usually an atmospheric pressure), the total driving force of $p_f - p_p + \Delta p_b$ works to move the water rightward.

Furthermore, when Δp_b is negative (typically, for the case $\theta_1(\text{hydrophilic}) < 90^o < \theta_2(\text{hydrophobic})$), water does not move rightwards until $p_f - p_p$ becomes equal to $-\Delta p_b$, which is called the critical pressure, p_{cb}.

In Case c), the water in the left pore is connected to a reservoir and the water in the right pore is connected to another reservoir as can be seen in Fig. 2-4.

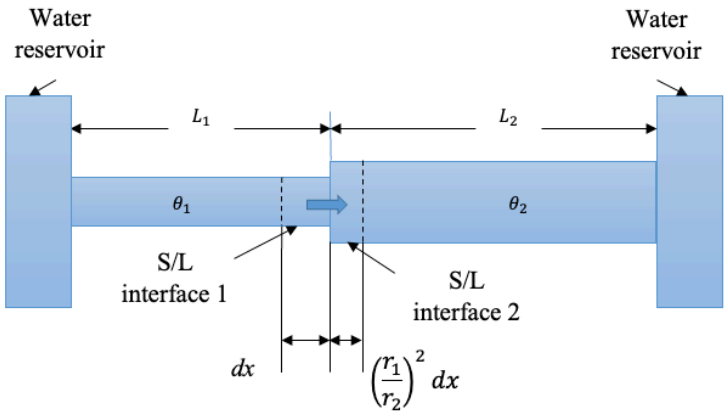

Fig. 2-4. Each of the left and right pores is connected to a large reservoir.

The contact is solid/liquid (s/l) before and after the movement of water. Then, the increase of surface energy is

$$2\pi r_2\left(\frac{r_1}{r_2}\right)^2 dx\sigma_{sl,2} - 2\pi r_1 dx\sigma_{sl,1} = 2\pi r_2\left(\frac{r_1}{r_2}\right)^2 dx\left(\sigma_{sg,2} - \sigma\cos\theta_2\right) - 2\pi r_1 dx\left(\sigma_{sg,1} - \sigma\cos\theta_1\right) = -\left(2\pi r_2\left(\frac{r_1}{r_2}\right)^2 dx\sigma\cos\theta_2 - 2\pi r_1 dx\sigma\cos\theta_1\right) + \left(2\pi r_2\left(\frac{r_1}{r_2}\right)^2 dx\sigma_{sg,2} - 2\pi r_1 dx\sigma_{sg,1}\right)$$

Or, in terms of energy decrease, it is

$$\left(2\pi r_2\left(\frac{r_1}{r_2}\right)^2 dx\sigma\cos\theta_2 - 2\pi r_1 dx\sigma\cos\theta_1\right) - \left(2\pi r_2\left(\frac{r_1}{r_2}\right)^2 dx\sigma_{sg,2} - 2\pi r_1 dx\sigma_{sg,1}\right)$$

Suppose the work of $\pi {r_1}^2 dx\Delta p_c$ is done by this energy release

$$\pi {r_1}^2 dx\Delta p_c = \left(2\pi r_2 \left(\frac{r_1}{r_2}\right)^2 \sigma \cos\theta_2 - 2\pi r_1 dx\sigma \cos\theta_1\right) - \left(2\pi r_2 \left(\frac{r_1}{r_2}\right)^2 dx\sigma_{sg,2} - 2\pi r_1 dx\sigma_{sg,1}\right) \tag{2-8}$$

Hence,

$$\Delta p_c = 2\sigma\left(\frac{\cos\theta_2}{r_2} - \frac{\cos\theta_1}{r_1}\right) - 2\left(\frac{\sigma_{sg,2}}{r_2} - \frac{\sigma_{sg,1}}{r_1}\right) \tag{2-9}$$

The difference between Δp_a in equation (2-5) and Δp_c in equation (2-9) is that $-2\left(\frac{\sigma_{sg,2}}{r_2} - \frac{\sigma_{sg,1}}{r_1}\right)$ is added in equation (2-9).

The difference between Δp_b in equation (2-7) and Δp_c in (2-9) is that $\frac{2\cos\theta_2}{r_2}$ in equation (2-7) becomes $\frac{\cos\theta_2}{r_2}$ in equation (2-9).

The total driving force is $p_f - p_p + \Delta p_c$, p_f and p_p are now the pressure in the left and right reservoir, respectively. Similar to Δp_b, Δp_c is negative typically for the case $\theta_1(\text{hydrophilic}) < 90^o < \theta_2(\text{hydrophobic})$, and water does not move rightwards until $p_f - p_p$ becomes equal to $-\Delta p_c$, which is called critical pressure, p_{cc}. It should also be noticed that Δp_{cc} is usually lower than Δp_{cb}, since $\frac{\cos\theta_2}{r_2}$ is negative.

For calculation of flow rate for the case c, first consider case b. When the pressure in the left reservoir is increased and $p_f - p_p$ becomes above Δp_{cb}, the water starts to move rightward and eventually reaches the right reservoir, and the meniscus disappears. Then, the equations for case c become applicable and the total driving force becomes $p_f - p_p + \Delta p_c$. The flow rate can be calculated by balancing the total driving force by the pressure drop due to the viscous flow.

The pressure drop in the left-side pore is written by the Poiseuille law as

$$\Delta p_1 = \frac{8\eta L_1 v_1}{r_1^2}$$

Similarly, in the right-side pore

$$\Delta p_2 = \frac{8\eta L_2 v_2}{r_2^2}$$

where η is the viscosity of water.

The overall pressure drop is, therefore,

$$\Delta p_1 + \Delta p_2 = \frac{8\eta L_1 v_1}{r_1^2} + \frac{8\eta L_2 v_2}{r_2^2} = \frac{8\eta L_1 v_1}{r_1^2}\left(1 + \left(\frac{L_2}{L_1}\right)\left(\frac{r_1}{r_2}\right)^4\right) \quad (2\text{-}10)$$

Balancing the total driving force by the pressure drop,

$$p_f - p_p + \Delta p_c = \Delta p_1 + \Delta p_2 \quad (2\text{-}11)$$

Combining equations (2-9), (2-10) and (2-11)

$$p_f - p_p + \Delta p_c = p_f - p_p + 2\sigma\left(\frac{\cos\theta_2}{r_2} - \frac{\cos\theta_1}{r_1}\right) - 2\left(\frac{\sigma_{sg,2}}{r_2} - \frac{\sigma_{sg,1}}{r_1}\right) = \frac{8\eta L_1 v_1}{r_1^2}\left(1 + \left(\frac{L_2}{L_1}\right)\left(\frac{r_1}{r_2}\right)^4\right)$$

(2-12)

Note that equation (2-12) indicates that the effect of the surface energy, σ_{sg}, is included in the equation. Normally, this effect is not very large for polymeric materials. But it is very large for metals.

Table 2-1 shows the solid/air interfacial tension, often called surface energy of solid, σ_{sg} for various polymers that are often used for membrane fabrication and stainless steel, as a typical example for metals.

Table 2-2. Surface energy σ_{sg} of polymers and stainless steel.

Polymer	Surface energy of solid, N/m
Polyacrylonitrile (PAN)	0.047 [a]
Polyethersulfone (PES)	0.047 [a]
Polyphenylene oxide (PPO)	0.046 [a]
Polysulfone (PS)	0.042 [a]
Cellulose acetate (CA)	0.0411 [a]
Polyurethane (PU)	0.038 [b]
Polyvinyl alcohol (PVA)	0.0365 [a]
Polyethylene (PE)	0.035 [a]
Polystyrene (PSt)	0.034 [b]
Polyvinylidene fluoride (PVDF)	0.0303 [a]
Polypropylene (PP)	0.0301 [a]
Polytetrafluoroethylene (PTFE)	0.019 [b]
Stainless steel (SS)	0.7-1.1[c]

[a] Solid surface energy (SEF) data for common polymers, http://www.surface-tension.de/solid-surface-energy.htm.
[b] Tristar Surface energy of plastics, https://www.tstar.com/blog/bid/33845/surface-energy-of-plastics
[c] Technibond surface energy chart, hrome-extension://efaidnbmnnnibpcajpcglclefindmkaj/https://www.technibond.co.uk/wp-content/uploads/2019/04/surface-energy-chart.pdf

2.4. Results and discussion

Justification of the model equation

Tian et al. derived a model equation to explain the experimental results of the anisotropic membrane that shows unidirectional water transport [15].

In Fig. 4 of their paper, Tian et al. showed the critical pressure, p_c, as a function of a parameter $k = \frac{d_0}{2r}$, assuming r = 100 μm for their calculation. They set the smallest k = 0.1 and k was progressively increased by 2 times, 4 times, and 6.9 times.

It is difficult to imitate a complicated water channel between two cylindrical bundles that is shown schematically in Fig. 2-1, with a cylindrical pore that is shown in Fig. 2-2 as the radius of the pore changes along the pore and d_0 is the narrowest part of pore and radius of fiber should be considered. Herein, however, we will calculate p_{cb} by equation (2-7). The results are then compared with the data given by Tian et al. in Fig. 2-5. The agreement looks very good.

It should be noted that p_c becomes negative when the asymmetric fabric is flipped, i.e., $\theta_1 = 170^{\circ}$ and $\theta_2 = 30^{\circ}$. This means that the spontaneous flow will take place when the hydrophobic surface is in contact with water, which also agrees with the experimental results of Wang et. al. [11], although Tian et al. reported positive p_cs for such a case.

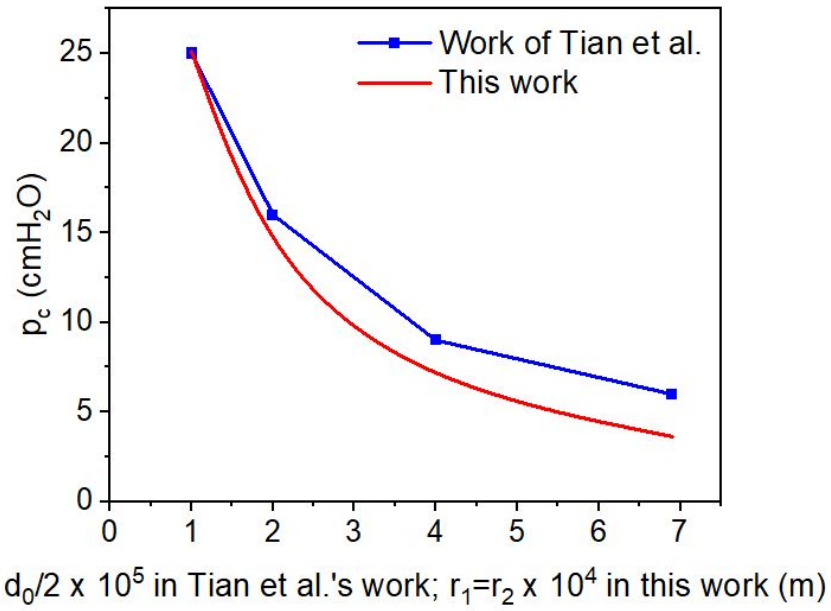

Fig. 2-5. Comparison of Tian et al.'s work (by their developed model) and the modeling result of this work. (Tian's data were taken from Fig. 4 of reference [15] with k=0.1 for magnification=1. The data for this work was calculated by equation (2-7) with r_1=r_2=100 μm for magnification=1).

Simulation results

Simulation was made using the following parameters that characterize the membrane:

$r_1 = r_2$ = 200 μm, L_1 = 46 μm, L_2 = 320 μm, θ_1 = 61°, θ_2 = 120°, σ_{sg1}=0.0411 N/m and σ_{sg2}=0.019 N/m.

The values for $r_1 = r_2$, L_1 and L_2 were chosen rather arbitrarily, but considering the geometry of various Janus membranes reported by Zhao et al. in their review paper [19]. θ_1 and σ_{sg1} of hydrophilic cellulose acetate (CA) and θ_2 and σ_{sg2} of hydrophobic polytetrafluoroethylene (PTFE) of the CA/PTFE Janus membrane prepared by Hou et al. [15] were typically chosen for the model simulation.

Fig. 2-6 shows the effect of $p_f - p_p$ on the flow rate.

a)

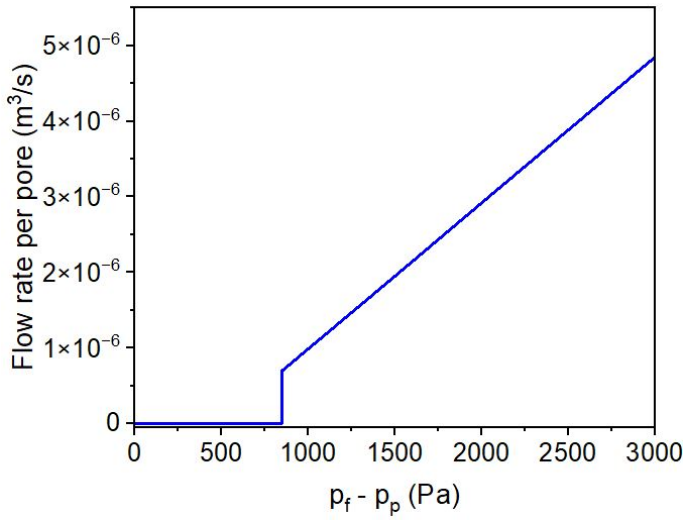

b)

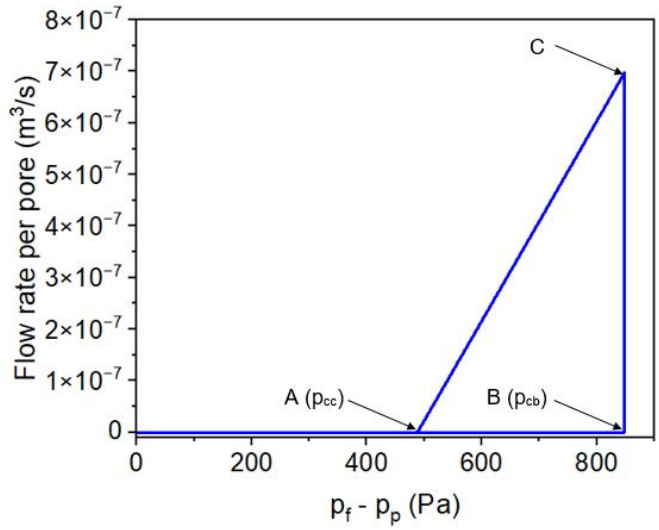

Fig. 2-6. Flow rate as a function of $p_f - p_p$ (Calculated by equation (2-12) with $r_1 = r_2 = 200$ μm, $L_1 = 46$ μm, $L_2 = 320$ μm, $\theta_1 = 61^o$, $\theta_2 = 120^o$, $\sigma_{sg1} = 0.0411$ N/m and $\sigma_{sg2} = 0.019$ N/m) a) flow rate for $p_f - p_p > p_{cb}$ b) flow rate for $p_f - p_p < p_{cb}$.

In Fig. 2-6 a), the flow rate is zero until the critical pressure of 848 Pa (p_{cb} calculated by equation (2-7)) is reached. Upon reaching the critical pressure the water starts to flow from the left to the

right pore where the meniscus is present (Fig. 2-3) until water enters into the reservoir 2 and the meniscus disappears (Fig. 2-4). In the absence of the meniscus, the driving force becomes $p_f - p_p + \Delta p_c$ and flow rate is calculated by equation (2-12). Note that a sudden jump of flow rate from zero to 6.97×10^{-7} m^3/s occurs at p_{cb}. Thereafter, the flow rate increases linearly with an increase in $p_f - p_p$ increases.

In Fig. 2-6 b), on the other hand, $p_f - p_p$ was reduced from p_{cb}, after both reservoirs were connected with water and the meniscus has disappeared (Case c). The flow rate is hence calculated by equation (2-12) and it decreases linearly until it reaches $p_{cc} = 488$ Pa, at which the flow rate becomes zero. A hysteresis loop forms when $p_f - p_p$ is changes from p_{cc} to p_{cb} and back to p_{cc} ($\mathrm{A} \rightarrow \mathrm{B} \rightarrow \mathrm{C} \rightarrow \mathrm{A}$).

Now the hydrophilicity/hydrophobicity of the pores is reversed, i.e. the left side is hydrophobic with $\theta_1 = 120^o$ (σ_{sg2}=0.019 N/m) and the right side is hydrophilic with $\theta_2 = 61^o$ (σ_{sg1}=0.0414 N/m). The other parameters remain the same as Fig. 2-6. The computational results are shown in Fig. 2-7. There is a flow from left to right with a flow rate of 9.42×10^{-7} m^3/s even when the pressure difference $p_f - p_p = 0$.

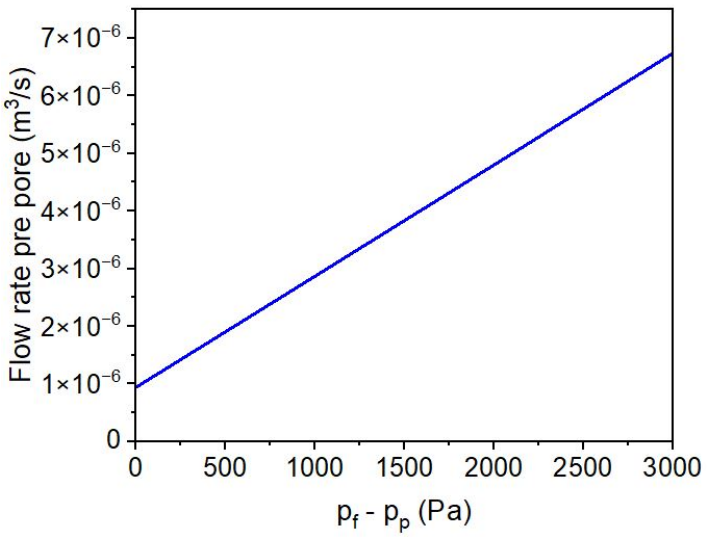

Fig. 2-7. Flow rate as a function of $p_f - p_p$ (Calculated by equation (2-12) with $r_1 = r_2 = 200$ μm, $L_1 = 46$ μm and $L_2 = 320$ μm, $\theta_1 = 120^o$, $\theta_2 = 61^o$, $\sigma_{sg1} = 0.019$ N/m and $\sigma_{sg2} = 0.0411$ N/m).

In Figs. 2-6 a) there is no flow when $p_f - p_p$ is less than 848 Pa, Thus the flow is directional when $0 < p_f - p_p < 848$ Pa.

Fig. 2-8 a) shows the effect of $p_f - p_p$ on the flow rate for the pore radii of 200, 300 and 400 × 10^{-6} m. Other parameters are the same as Fig. 2-6 a), i.e. the left is hydrophilic ($\theta_1 = 61^o$) and the right is hydrophobic ($\theta_2 = 120^o$). In the figure p_{cb} decreases and flow rate increases as pore radius increases. Fig. 2-8 b) shows the effect of $p_f - p_p$ on the flow rate, when the hydrophilicity/hydrophobicity is reversed. Similar to Fig. 2-7, Fig. 2-8 b) shows that there is water flow even when $p_f - p_p = 0$.

a)

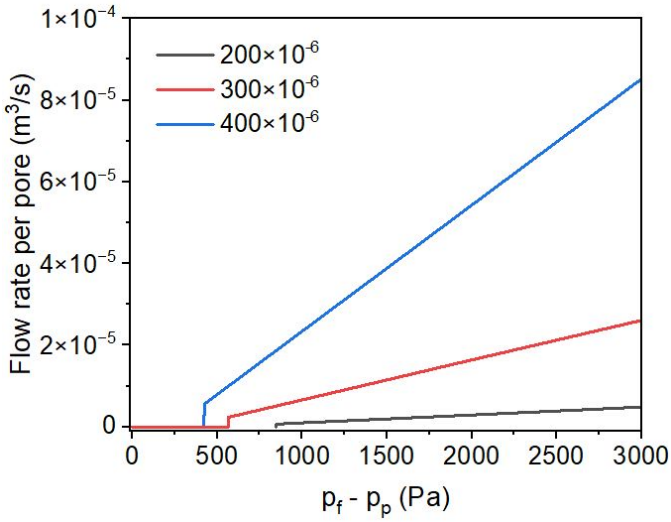

b)

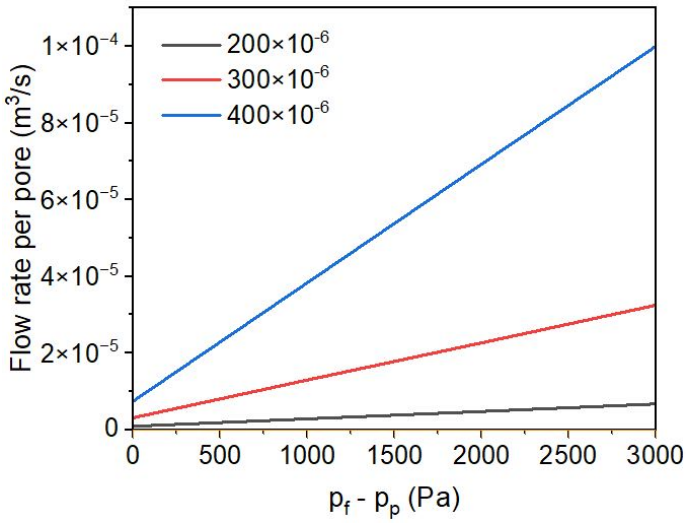

Fig. 2-8. Flow rate as a function of $p_f - p_p$ (Calculated by equation (2-12) with $r_1 = r_2 = 200$, 300 and 400 μm, $L_1 = 46$ μm and $L_2 = 320$ μm) a) $\theta_1=61^o$, $\theta_2=120^o$, $\sigma_{sg1}=0.0411$ N/m and $\sigma_{sg2}=0.019$ N/m, b) $\theta_1=120^o$, $\theta_2=61^o$, $\sigma_{sg1}=0.019$ N/m and $\sigma_{sg2}=0.0411$ N/m.

Fig. 2-9 shows the effect of reducing the pore radius from 200 μm of Fig. 2-6 a) to 20 μm either on the right side (Fig. 2-9 a)) or on the left side (Fig. 2-9 b)). All other parameters are the same as Fig. 2-6 a). Compared to Fig. 2-6 a), the flux is remarkably lower (3 orders of magnitude for Fig.

2-9 a) even for 10 times higher $p_f - p_p$, and 3 orders of magnitude for Fig. 2-9 b) at comparable $p_f - p_p$).

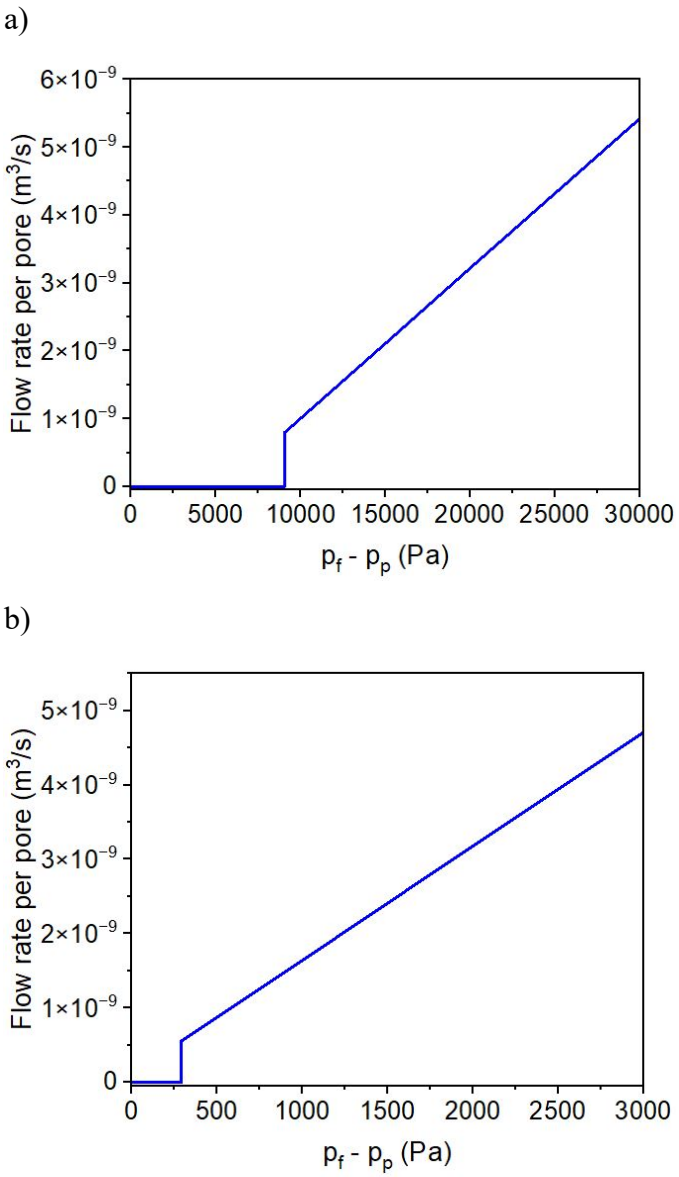

Fig. 2-9. Flow rate as a function of $p_f - p_p$ (Calculated by equation (2-12) with L_1 = 46 μm and L_2 = 320 μm, θ_1=61°, θ_2=120°, σ_{sg1}=0.0411 N/m and σ_{sg2}=0.019 N/m) a) r_1=200 and r_2=20 μm b) r_1=20 and r_2=200 μm).

Comparing Figs. 2-9 a) and 2-9 b), the flux of 2-9 a) is much lower, which is natural since the longer right side pore is narrowed in Fig. 2-9 a). It is interesting to note that p_{cb} at which the flux

jumps, is much larger in Fig. 2-9 a) (9040 Pa) than Fig. 2-9 b) (291 Pa). Thus, narrowing the right side pore leads to a broader range of the directional flow at a cost of the flux decrease.

Then, the effect of reversing the pore lengths of Fig. 2-6 a) was examined, i.e. the left side pore and right side pores were 320 μm and 46 μm, respectively. Other parameters remained the same. It was found that the simulation results were unchanged from Fig. 2-6 a). Similarly, reversing the pore lengths of Fig. 2-7 did not change the results shown in Fig. 2-7. Thus, reversing of the pore lengths does not affect the water flux.

In Fig. 2-10, the contact angle and surface energy were changed from Fig. 2-8. In Fig. 2-10 a), θ_1 is 10° (with $\sigma_{sg1} = 0.0365\ \mathrm{N/m}$) and θ_2 is 89° (with $\sigma_{sg2} = 0.0303\ \mathrm{N/m}$). The former surface properties are those of polyvinyl alcohol (PVA) and the latter those of PVDF. Unlike, Fig. 2-8 a) the sudden jump of the flux at p_{bc} is hardly observable in Fig. 2-10 a). This is because θ_2 is very close to 90°. (Actually, due to the larger value of p_{cc} than p_{bc}, the flow rate becomes negative at p_{bc}, but this effect is hardly seen in Fig. 2-10 a). In Fig. 2-10 b), there are positive flow rates even at $p_f - p_p = 0$, similar to Fig. 2-8 b).

a)

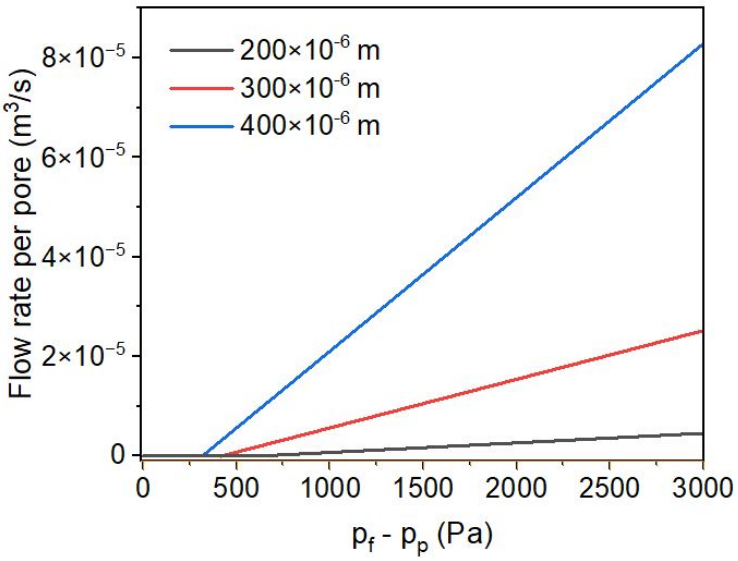

b)

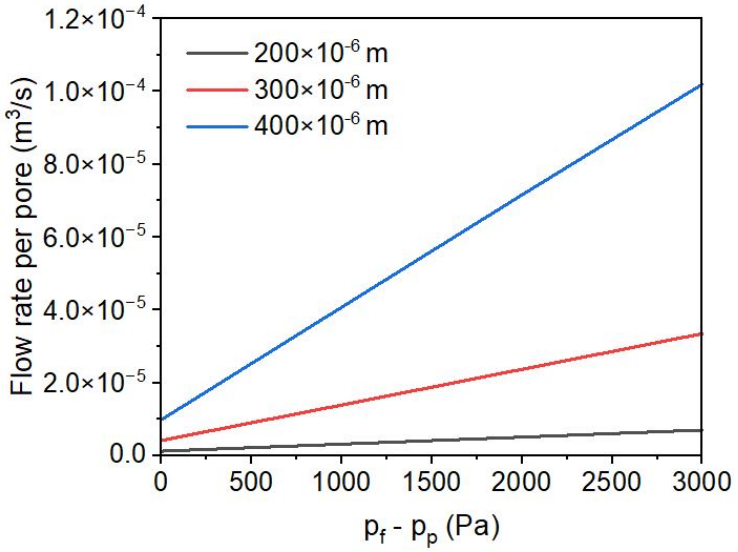

Fig. 2-10. Effect of $p_f - p_p$ on flow rate (Calculated by equation (2-12) with $r_1 = r_2 = 200$, 300 and 400 μm, $L_1 = 46$ μm and $L_2 = 320$ μm) a) $\theta_1=10^o$, $\theta_2=89^o$, $\sigma_{sg1}=0.0365$ N/m and $\sigma_{sg2}=0.0303$ N/m, b) $\theta_1=89^o$, $\theta_2=10^o$, $\sigma_{sg1}=0.0303$ N/m and $\sigma_{sg2}=0.0365$ N/m.

Fig. 2-11 a) shows the effect of the change of r_2 on the critical pressure p_{cb} while r_1 is kept constant at 400 μm. In Series 1, the left pore is hydrophilic, and the right is hydrophobic. p_{cb} is positive and decreases as r_2 increases. In Series 2, the left pore is hydrophobic, and the right is hydrophilic. p_{cb} is negative and slightly increases as r_2 increases. Therefore, the flow is directional in the pressure range between Series 1 and Series 2.

Fig. 2-11 b) shows the effect of the change of r_1 on the critical pressure p_{cb} while r_2 is kept constant at 400 μm. The flow is directional also in this case. In Series 1 p_{cb} is positive and almost constant, while in Series 2 p_{cb} is negative and increases as r_2 increases.

a)

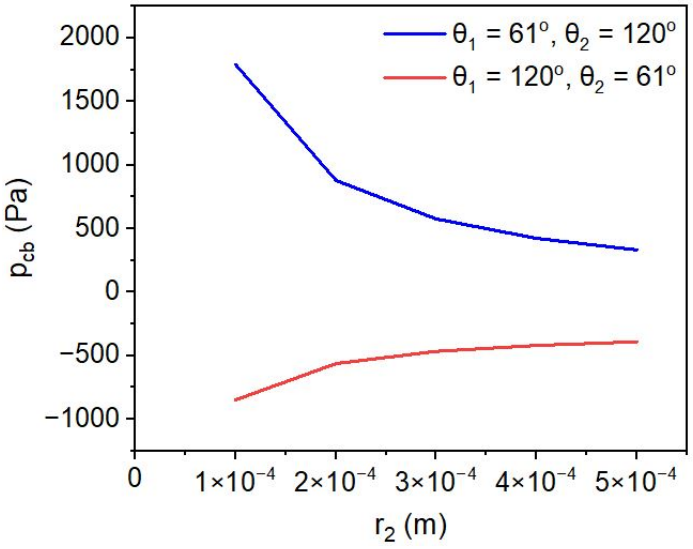

b)

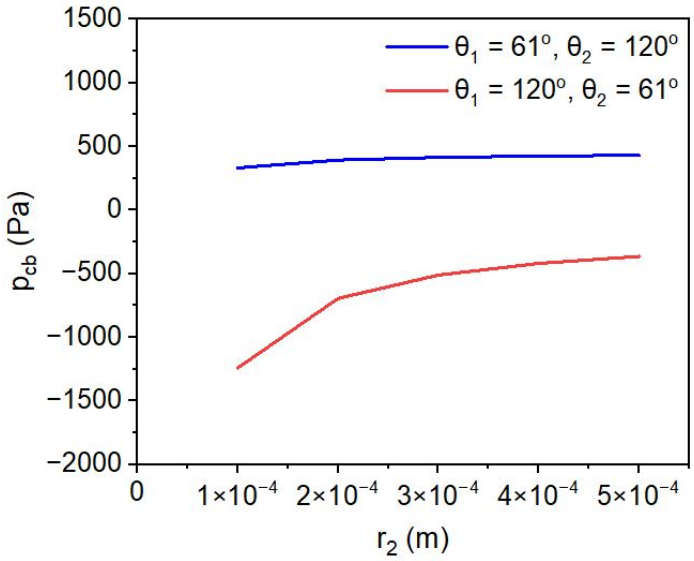

Fig. 2-11. Effect of pore radius on critical pressure, p_{cb} (L_1 = 46 μm, L_2 = 320 μm) a) Effect of change in r_1, r_2 = 400 μm, Series 1 (blue line): $\theta_1 = 61^o$, $\theta_2 = 120^o$, σ_{sg1}=0.0411 N/m and σ_{sg2}=0.019 N/m, Series 2 (red line): $\theta_1 = 120^o$, $\theta_2 = 61^o$, σ_{sg1}=0.019 N/m and σ_{sg2}=0.0411 N/m, b) Effect of change in r_1, r_2 = 400 μm, Series 1 (blue line): $\theta_1 = 61^o$, $\theta_2 = 120^o$, σ_{sg1}=0.0411 N/m and σ_{sg2}=0.019 N/m, Series 2 (red line): $\theta_1 = 120^o$, $\theta_2 = 61^o$, σ_{sg1}=0.019 N/m and σ_{sg2}=0.0411 N/m.

Equations (2-7), (2-9) and (2-12) imply the effect of the surface energy, σ_{sg}, on p_{cb}, p_{cc} and the flow rate. It is known that σ_{sg} of the metal surface is orders of magnitude higher than that of the polymer surface, although metal's contact angle is not very different from polymer. To know the effect of large σ_{sg}, a simulation was made for Janus membranes in which the hydrophilic layer was made of stainless steel while the hydrophobic layer was made of hydrophobic PTFE.

In Fig. 2-12 a), the left pore is made of hydrophilic stainless steel and the right pore PTFE. Interestingly, there is a flow when $p_f - p_p = 0$ even though the hydrophilic layer is at the left. On the other hand, there is no water flow in a $p_f - p_p$ range between 0 and $p_{cb} = 9060$ Pa, when stainless steel is on the right side. Above the p_{cb}, the flow rate increases linearly with an increase in $p_f - p_p$. Another effect of the use of stainless steel is that p_{cb} is an order of magnitude higher than cellulose acetate/polytetrafluoroethylene combination and the flow rate is also an order of magnitude higher, because of the high $p_f - p_p$, which is required to allow water flow.

a)

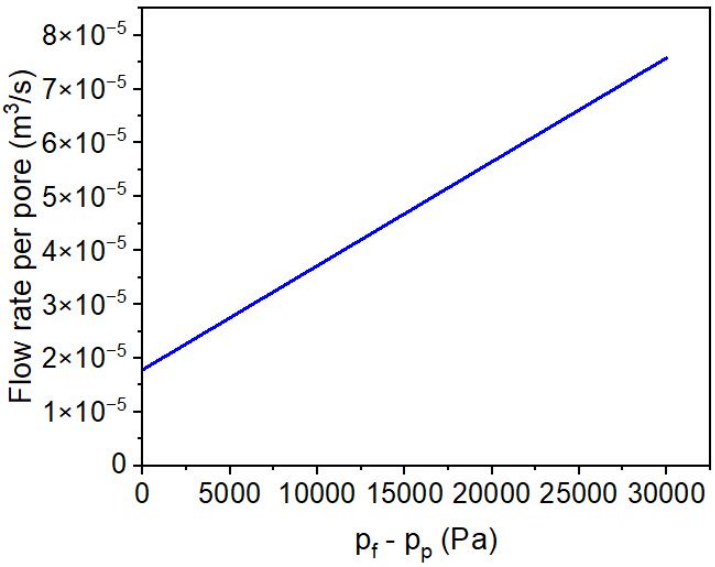

b)

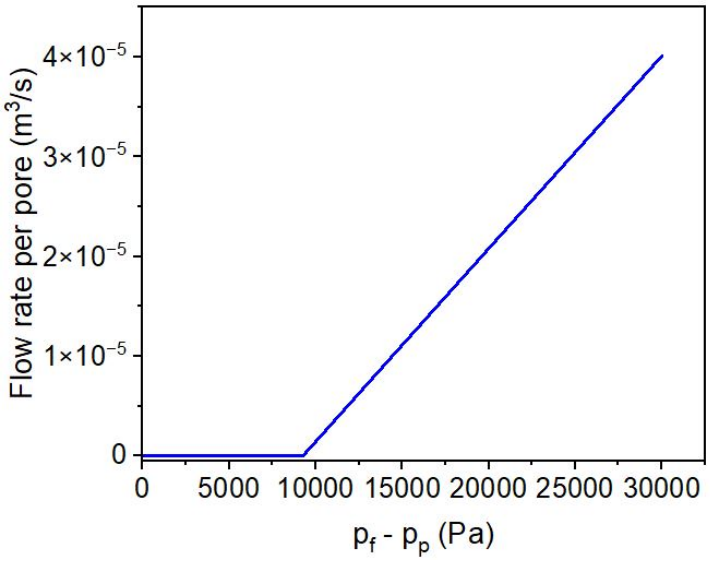

Fig. 2-12. Effect of $p_f - p_p$ on flow rate for PTEF/SS Janus membrane (Calculated by equation (2-10) with $r_1 = r_2 = 200$ μm, $L_1 = 46$ μm and $L_2 = 320$ μm): a) θ_1=74.2°, θ_2=120°, σ_{sg1}=1.0 N/m and σ_{sg2}=0.019 N/m, b) θ_1=120°, θ_2=74.2°, σ_{sg1}=0.019 N/m and σ_{sg2}=1.0 N/m.

Table 2-3 lists the LEP of the hydrophobic layer of Janus membrane as well as the P_{cb} of Janus membranes of two different configurations with the hydrophilic and hydrophobic layers having contact angles of 61° and 120°, respectively. The LEP is calculated based Young Laplace equation as can be seen in equation (2-13):

$$LEP = \frac{-2\sigma \cos\theta}{r_{max}} \tag{2-13}$$

where σ ($^{N}/_{m}$), θ (°) and r_{max} (m) are liquid surface tension, contact angle between membrane and wetting liquid, and maximum pore radius in the membrane, respectively.

The two configurations are 1) with the hydrophilic layer facing the reservoir and hydrophobic layer facing the permeate tank (the hydrophilic/hydrophobic configuration) and 2) with the hydrophobic layer facing the reservoir and hydrophilic layer facing the permeate tank (the hydrophobic/hydrophilic configuration). As shown in Table 2-3, the absolute values of LEP and P_{cb} are proportional with the reciprocal of pore radius. It is interesting to notice that for the hydrophobic/hydrophilic configuration, the P_{cb} has the opposite sign to the corresponding LEP, indicating spontaneous water flow across the interface. On the other hand, for the hydrophilic/hydrophobic configuration, the P_{cb} has the same sign but more than doubling the value of the corresponding LEP, representing the need of an increased transmembrane pressure to overcome the critical pressure for water to flow across the interface to enter the pore of the hydrophobic layer. In other words, a hydrophilic/hydrophobic Janus would be able to prevent pore wetting of its hydrophobic layer for transmembrane pressure more than doubling its LEP.

Table 2-3. P_{cb} of Janus membrane and LEP of hydrophobic layer at different pore sizes when the contact angles of hydrophilic and hydrophobic layer were 61° and 120°, respectively.

***r* (µm)**	**LEP (kPa)** hydrophobic	**P_{cb} (kPa)** hydrophilic/hydrophobic	**P_{cb} (kPa)** hydrophobic/hydrophilic
0.2	360.00	848.06	-837.13
2.0	36.00	84.81	-83.71
20.0	3.60	8.48	-8.37
200.0	0.36	0.85	-0.84

2.5. Conclusions

From this work, the following conclusions are drawn.

1. The novel transport model based on the Young equation explains the directional transport of the Janus membranes, i.e. water flows spontaneously from the hydrophobic to the hydrophilic side of the membrane but a critical pressure should be overcome to allow the water to flow from the hydrophilic to the hydrophobic side of the membrane. The model can calculate critical pressure which is really important because it helps to understand the water transport within the pores of Janus membranes to design membranes.
2. For the hydrophilic/hydrophobic configuration, the critical pressure is more than doubling the Liquid Entry Pressure (LEP) of its hydrophobic layer, confirming the ability of Janus membrane of such a configuration to significantly enhance pore wetting prevention in Membrane distillation.

3. The model is able to calculate water flux in the pore of Janus membranes for the first time, which also can explain the flux enhancement that occurs when a hydrophobic layer is coated on top of a hydrophilic substrate.
4. The surface energy of the membrane material should be considered to evaluate the driving force for the water flow of the Janus membrane unlike the movement of water driven by the capillary force working between two menisci.
5. The model predicts the presence of the hysteresis loop in the flow rate/pressure plot of the Janus membrane.
6. The model predicts high critical pressure and high flow rate for metal/polymer bilayer membranes due to an order of magnitude larger surface energy of the metal.

2.6. References

[1] H. Yang, Y. Xie, J. Hou, A.K. Cheetham, V. Chen, S.B. Darling. Janus Membranes: Creating Asymmetry for Energy Efficiency. Advanced Materials 2018;30. https://doi.org/10.1002/adma.201801495.

[2] L. Meng, W. Shi, Y. Li, X. Li, X. Tong, Z. Wang, Janus membranes at the water-energy nexus: A critical review, Adv. Colloid Interface Sci. 318 (2023) 102937. https://doi.org/10.1016/j.cis.2023.102937.

[3] O. Makanjuola, F.E. Ahmed, I. Janajreh, R. Hashaikeh, Development of a dual-layered PVDF-HFP/Cellulose membrane with dual wettability for desalination of oily wastewater, J. Membr. Sci. 570 (2018) 418-426. DOI: 10.1016/j.memsci.2018.10.028.

[4] S. Zhao, Z. Tao, M. Han, Y.-X. Huang, B. Zhao, L. Wang, X. Tian, F. Meng, Hierarchical Janus membrane with superior fouling and wetting resistance for efficient water recovery from challenging wastewater via membrane distillation, J. Membr. Sci. 618 (2021) 118676. https://doi.org/10.1016/j.memsci.2020.118676.

[5] L. Zou, P. Gusnawan, G. Zhang, J. Yu, Novel Janus composite hollow fiber membrane-based direct contact membrane distillation (DCMD) process for produced water desalination, J. Membr. Sci.597 (2020) 117756. https://doi.org/10.1016/j.memsci.2019.117756.

[6] M. Han, T. Dong, D. Hou, Y. Jingmei, L. Han, Carbon nanotube based Janus composite membrane of oil fouling resistance for direct contact membrane distillation, J. Membr Sci. 607 (2020) 118078. DOI: 10.1016/j.memsci.2020.118078.

[7] R. Zhang, Y. Sun, Z. Guo, W. Liu, Janus membranes with asymmetric wettability applied in oil/water emulsion separations, Adv. Sustainable Syst. (2021) 2000253. DOI: 10.1002/adsu.202000253.

[8] B. Bhushan, Bioinspired oil-water separation approaches for oil spill clean-up and water purification, Phyl. Trans. R. Soc. A 377: 20190120. http://dx.doi.org/10.1098/rsta.2019.0120.

[9] X. Lin, J. Heo, M. Choi, J. Hong, Simply realizing durable dual Janus superwettable membranes integrating underwater low-oil-adhesive with super-water-repellent surfaces for controlled oil–water permeation, J. Membr. Sci. 580 (2019) 248-255. https://doi.org/10.1016/j.memsci.2019.03.038.

[10] H.-N. Li, J. Yang, Z.-K. Xu, Hollow fiber membranes with Janus surfaces for continuous deemulsification and separation of oil-in-water emulsions, J. Membr. Sci. 602 (2020) 117964. https://doi.org/10.1016/j.memsci.2020.117964.

[11] Y. Lin, M. S. Salem, L. Zhang, Q. Shen, A.H. El-shazly, N. Nady, H. Matsuyama, Development of Janus membrane with controllable asymmetric wettability for highly-efficient oil/water emulsions separation, J. Membr. Sci. 606 (2020) 118141. https://doi.org/10.1016/j.memsci.2020.118141.

[12] H. Wang, J. Ding, L. Dai, X. Wang, T. Lin, Directional water-transfer through fabrics induced by asymmetric wettability, J. Mater. Chem, 20 (2010) 7938-7940. DOI: 10.1039/c0jm02364g.

[13] Y. Liang, S. Kim, P. Kallem, H. Choi, Capillary effect in Janus electrospun nanofiber membrane for oil/water emulsion separation, Chemosphere 221 (2019) 479-485. https://doi.org/10.1016/j.chemosphere.2019.01.048.

[14] C. Yang, N. Han, C. Han, M. Wang, W. Zhang, W. Wang, Z. Zhang, W. Li, X. Zhang, Design of a Janus F-TiO_2@PPS porous membrane with asymmetric wettability for switchable oil/water separation, ACS Appl. Mater. Interfaces 11(2019) 22408-22418. https://doi.org/10.1021/acsami.9b05191.

[15] L. Hou, N. Wang, X. Man, Z. Cui, J. Wu, J. Liu, S. Li, Y. Gao, D. Li, L. Jiang, Y. Zhao, Interpenetrating Janus membrane for high rectification ratio liquid unidirectional penetration, ACS Nano 13 (2019) 4124-4132. https://doi.org/10.1021/acsnano.8b08753.

[16] X. Tian, J. Li, X. Wang, Anisotropic liquid penetration arising from a cross-sectional wettability gradient, Soft Matter 8 (2012) 2633-2637. DOI: 10.1039/c2sm07111h.

[17] L. Zoka, R.M. Narbaitz, T. Matsuura, Effect of surface modification with electrospun nanofibers on the performance of an ultrafiltration membrane, J. Membr. Sci. Res. 6 (2020) 351-358. DOI: 10.22079/JMSR.2020.119481.1319.

[18] K.M. Dobosz, C.A. Kuo-Leblanc, T.J. Martin, D.J. Schiffman, Ultrafiltration membranes enhanced with electrospun nanofibers exhibit improved flux and fouling resistance, Ind. Eng. Chem. Res. 56 (2017) 5724–5733. https://doi.org/10.1021/acs.iecr.7b0063.

[19] Y. Zhao, H. Wang, H. Zhou, T. Lin, Directional fluid transport in thin porous materials and its functional applications, Small 13 (2017) 1601070.

Chapter 3: 3D morphology-based analysis for liquid entry pressure estimation

Chapter 3 contains an adapted version of the manuscript that will be submitted to a peer-reviewed journal soon.

Estimation of liquid entry pressure of hydrophobic membranes using 3D morphology-based machine learning approach

Alireza Chamani[a], Arash Rabbani[b], Takeshi Matsuura[a], Dipak Rana[a], Christopher Q. Lan[a]

[a]*Department of Chemical and Biological Engineering, University of Ottawa, 161 Louis Pasteur Private, Ottawa, Ontario K1N 6N5, Canada*

[b]*School of Computing, University of Leeds, Leeds, LS2 9JT, UK*

3.1. Abstract

Water scarcity is a critical challenge in today's world. One solution to overcome this challenge is desalination. The state-of-the-art technology for desalination is reverse osmosis (RO), however; RO is incapable of desalinating brines with high concentrations. Membrane distillation (MD) is a technology that allows desalination of highly saline brines. However, MD has not been fully commercialized, mainly due to wetting phenomena in the pores of the membranes. The parameter to evaluate the suitability of a membrane for MD in terms of pore wetting is called liquid entry pressure (LEP). There are a few models that can estimate LEP; however, they are mainly developed based on ideal cylindrical pores. In this study, we have developed a model that uses the 3D image of the membrane to estimate LEP very quickly, allowing us to consider the real structure of the membrane when estimating LEP. The model was also validated using experimental data, and the effect of different membrane properties, such as pore size, and throat size, on LEP was studied.

3.2. Introduction

Water is a vital component required by all living beings on Earth to survive, especially freshwater which has an important role in human development [1,2]. Water shortage has become a global crisis recently [3]. Changes in living standards, living cultures, and increasing population increased demand for freshwater and its withdrawals. Nowadays, one out of every three people lacks access to freshwater [4]. Saline water accounts for over 97% of global water resources, while freshwater comprises only less than 3% [5]. Only 0.06% of accessible freshwater is readily available, with the remainder being comprised of groundwater, and reservoirs such as frozen polar ice caps or glaciers [6]. To address the growing need for freshwater, the first desalination facilities were set up in the late 1950s [5,7]. Due to the availability of inexpensive fossil fuels in the past, the earliest technologies were thermally based. However, with the increase in energy prices, research focused on enhancing the energy efficiency of commercial technologies and proposing new approaches [7]. Particularly, the popularity of membrane desalination has increased due to advancements in materials and reductions in costs. One of the most effective techniques for desalting saltwater in terms of energy consumption is reverse osmosis (RO) [8]. Over the past sixty years, RO membrane technology has advanced, now constituting 44% of the global desalination output capacity and being utilized in 80% of desalination facilities worldwide [9]. However, despite its advanced level, RO technology is not adequate for desalinating high-salinity brines. Due to the relationship between osmotic pressure and solute concentration, high-salinity RO desalination requires extremely high hydraulic pressure to counteract the osmotic pressure differential across the membrane [8]. High hydraulic pressure causes membrane compaction or deformation, which leads to a decrease in membrane water permeability [10]. The osmotic pressure equation is as follows [11]:

$$\Pi = icRT \tag{3-1}$$

where Π, i, c, R, and T are osmotic pressure, van't Hoff index, molar concentration, ideal gas constant, and temperature, respectively.

Membrane distillation (MD) is another membrane-based thermal desalination technique that involves the passing of only vapour molecules through a porous hydrophobic membrane driven by the vapor pressure gradient across the membrane. This method is promising in the treatment of highly saline streams, with salt concentrations ranging from approximately 70 to 300 g salt/kg solution [12, 13]. MD has several appealing advantages, including lower operating temperatures compared to traditional thermal processes, wherein the solution, predominantly water, does not need to be heated to reach the boiling point [12]. Despite the benefits of MD, large-scale commercialization of this process has not happened yet, and the main reasons are high energy consumption, low permeate flux, and pore wetting. When the liquid enters into the pores instead of vapor, pore wetting occurs. Pore wetting limits process effectiveness, by causing reduced separation efficiency and inhibiting continuous operation [14]. The resistance of a membrane to wetting can be measured through its liquid entry pressure (LEP), indicating the highest pressure of liquid feed that the membrane can endure before becoming wet [15]. Accurate estimation of LEP is necessary to evaluate the membrane's potential for wetting resistance since wetting phenomena are mostly caused by exceeding the LEP [16]. Fig. 3-1a illustrates the schematic of a classic setup for LEP measurement [16]. There are several models which have been presented to estimate LEP. The first model for LEP estimation is the Young-Laplace model which considers pores as ideal cylinders (Fig. 3-1b), and is described by [16]:

$$LEP = \frac{-2\sigma \cos\theta}{r_{max}} \tag{3-2}$$

where σ ($^{N}/_{m}$), θ (°) and r_{max} (m) are liquid surface tension, contact angle between membrane and wetting liquid, and maximum pore radius in the membrane, respectively. A modified model is Franken's model which includes another parameter, B $(-)$, which is the pore geometry coefficient, and the value of B is determined by the form of the pore cross-section. For a circular cross-section pore, it is equal to one. The Franken's model is described by [17]:

$$LEP = \frac{-2B\sigma \cos\theta}{r_{max}} \tag{3-3}$$

Another model was developed by Kim et al. [18], in which the pores were no longer described as ideal cylinders considered in the Young-Laplace model but as tori instead (Fig. 3-1c); membranes were described as arrays of uniform fibers intersecting at constant angles. The equation for the pressure difference (ΔP) at the liquid-gas interface at the membrane surface was developed as follows [15]:

$$\Delta P = \frac{2\sigma}{r}\frac{\cos(\theta-\alpha)}{1+(^{R}/_{r})(1-\cos\alpha)} = \frac{2\sigma}{r}\cos\theta_{eff} \tag{3-4}$$

where θ (°), σ ($^{N}/_{m}$), r (m), θ_{eff} (°), R (m), and α (°) are contact angle, surface tension, pore radius, effective contact angle, fiber radius, and structural angle. The structural angle denotes the axial deviation of the pores and can be derived by [15]:

$$\sin(\theta-\alpha) = \frac{\sin\theta}{1+(^{r}/_{R})} \tag{3-5}$$

A modification to Kim's model was done by Servi et al. by defining a new parameter, h, which is the distance between the floor and the bottom of the pore's fibers (Fig. 3-1d). This metric indicates a positive value when there exists a space between the fibers and the floor, and a negative value when the floor surpasses the base level of the fibers [19]. The drawback of this model is that

estimating R/r is too difficult. Additionally, the model was only used for fibrous nylon membranes [16].

Yazgan-Birgi et al. developed a two-dimensional computational fluid dynamics (CFD) to estimate the LEP of hydrophobic membranes based on the volume of fluid (VOF) approach [20]. They assumed the pore as an ideal cylinder, so this model suffers from inaccuracy due to simplifying the structure of membranes like the previous models. The real structure of a membrane is much more complex and usually does not follow a simple pattern as you can see in Fig. 3-1e. Recently, Jäger et al. developed a CFD model in which the Shan and Chen multiphase model was used to simulate LEP using multiphase flow at the pore level for 3D structures [21]. However, the main challenge in their model was the considerable time required for simulation [21].

The objective of this work was to develop a morphology-based model, based on the approach presented in [22], to estimate LEP rapidly (in the order of a few minutes). In this study, a MATLAB code was developed to process 3D binary images of membranes and estimate LEP. To validate the model, the Gore membrane (PT20) was studied and the estimated LEP for this membrane was compared to the experimentally measured LEP. After model validation, the effects of different parameters such as pore size, and throat size on LEP were examined. For this purpose, we developed different codes in the MATLAB environment, allowing us to estimate the above-mentioned membrane properties from 3D images of membranes.

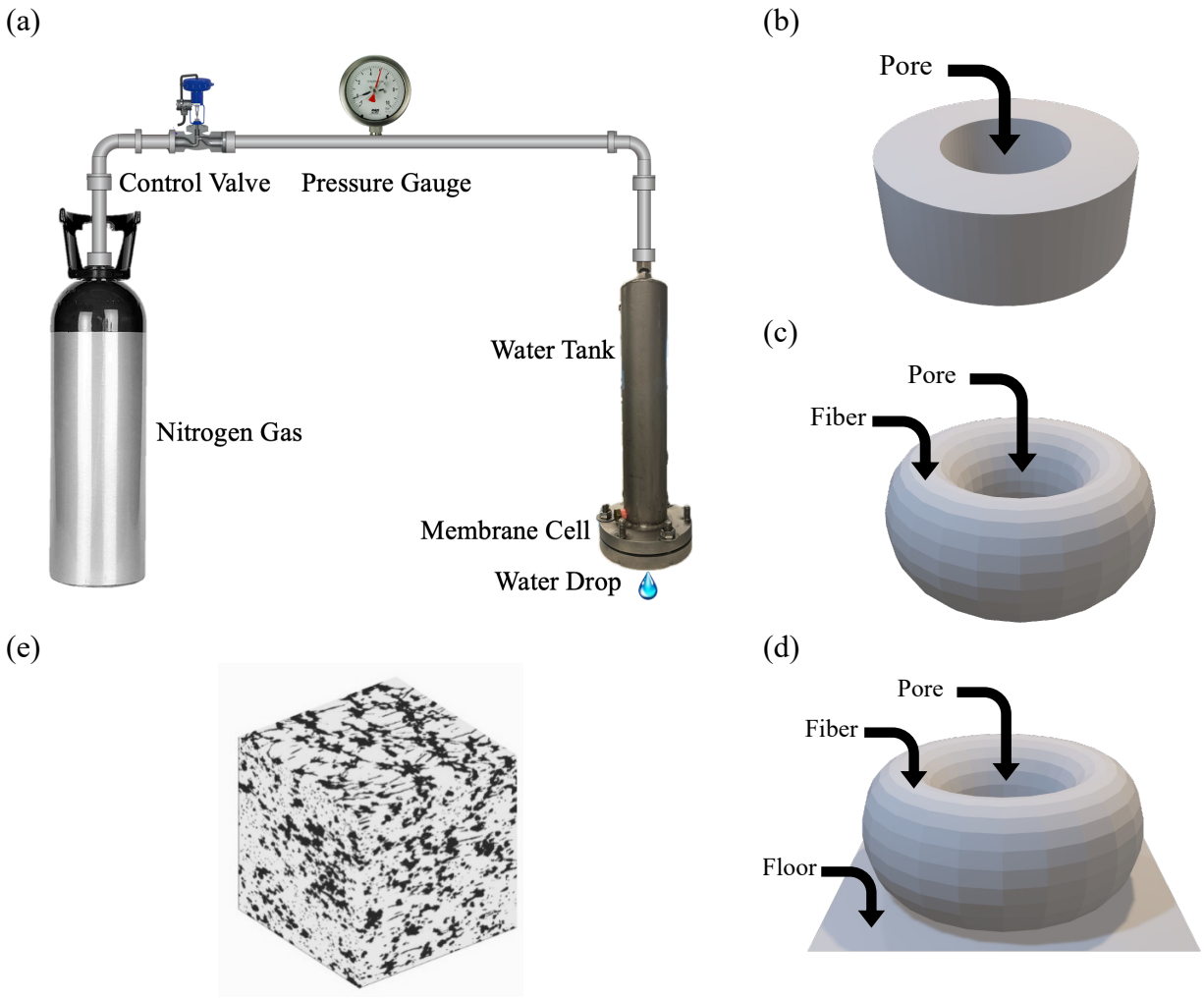

Fig. 3-1. (a) Schematic of a classic setup for LEP estimation; Schematic of a membrane pore based on: (b) Young-Laplace model (cylindrical pore), (c) Kim model (toroidal pore), (d) Servi model (toroidal pore and floor bottom of the fibers); (e) A real structure of PTFE membrane (FGLP14250).

3.3. Materials and methods

3.3.1. Materials

In this study, we used the reported data [23,24] (experimental LEP and contact angle) and 3D image [25] from the previously published literatures, of PT20 membrane, manufactured by Gore Inc. PT20 is a hydrophobic membrane made of polytetrafluoroethylene (PTFE) with a pore size of 0.2 μm [23]. Cramer et al. utilized ptychographic X-ray computed tomography to capture 3D images, and the equipment employed by Cramer et al. was coherent Small-Angle X-ray Scattering (cSAXS) beamline at the Swiss Light Source, Paul Scherrer Institute, Switzerland [25]. The segmented images were presented in their report [25], and we analyzed the 3D image prepared by them.

3.3.2. Membrane LEP estimation

We developed a model to estimate LEP in the MATLAB environment version R2024a. The inputs of the model are the 3D binary image of the membrane, contact angle, and surface tension. At first, a large pore radius is chosen, then, it starts reducing the radii from the largest found (which will be accompanied by increasing pressure). By using the pore radii and the contact angle, the model predicts the location of the liquid using a morphology-based function and checks if the liquid is connected to the surface. When the liquid reaches the bottom of the membrane, the pressure in that state is called LEP.

3.3.3. Membrane properties

In this report, maximum pore size, mean pore size, and throat size are studied. Throat refers to the narrowest part of the pores that connect larger pore spaces within the membrane structure (Fig. 3-2) [26].

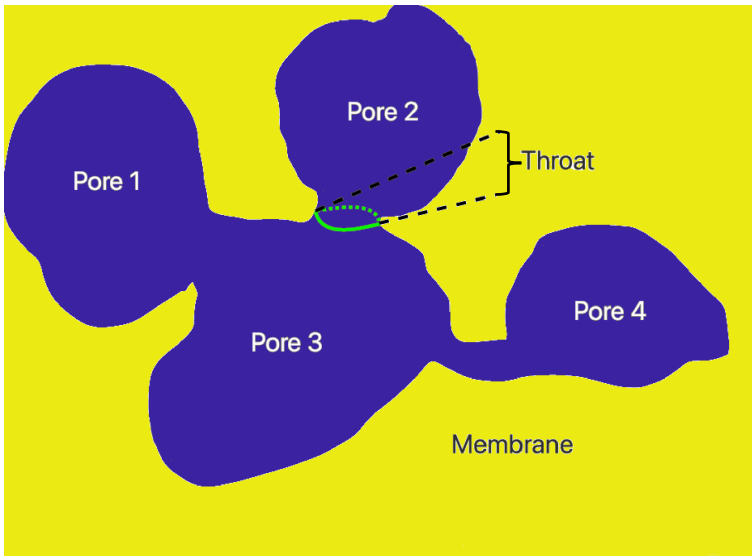

Fig. 3-2. Schematic of throats between two main pores.

3.4. Results and discussion

3.4.1. Morphology-based analysis for LEP estimation

This study implements a morphology-based approach to estimate the LEP of hydrophobic membranes using their 3D binary images. The method, inspired by Hilpert and Miller [22], models capillary-governed fluid displacement while simultaneously satisfying both the contact angle and surface curvature conditions. The surface was assumed to be smooth and there is no roughness.

The core principle of this approach is based on the Young-Laplace equation, which relates the pressure difference across a fluid interface to its surface tension and curvature:

$$P = \frac{-2\,\sigma\,cos\,\theta}{r_{max}} \tag{3-6}$$

where P is the pressure difference, σ is the interfacial tension, θ is the contact angle, and r is the radius of curvature (Fig. 3-3a). From an image processing point of view, creating a water space that touches the solid space with a contact angle of 0 and curvature of r is trivial and can be done through pore-space image opening using a spherical structuring element. However, for any other contact angle, the process is challenging. As suggested by Hilpert and Miller, we can synthetically modify the surface to adapt to the other contact angles. In this instance, we propose dilating the solid space, and then by dilating the water space subsequently, the desired contact angles can be reached. The key is to select the correct amount of dilation at each stage (*d:* dilation radius of solid phase, and *r:* dilation radius of water phase). Based on Fig. 3-3a, it can be seen that $\theta' = 180 - \theta$, $d = r \times sin(\alpha)$ and considering that $\alpha + \theta' = 90$, it can be written:

$$d = r \times cos(\theta') \tag{3-7}$$

The proposed algorithm operates on a 3D binary image of the membrane structure, where the solid phase is represented by 1 and the pore space by 0 (Fig. 3-3b). The process can be described by the following pseudo-code:

Initialize:

A = 3D binary image of the membrane (0: pore, 1: solid)

D = distance transform of A

Res = spatial resolution of the image

θ = contact angle

σ = interfacial tension

r_{max} = *maximum value in D*

Calculate $\theta' = 180 - \theta$

For r from r_{max} *to 1, step -1:*

Calculate $d = r \times \cos(\theta')$

Dilate solid space:

Use spherical structuring element of radius d

B = dilate (A, sphere(d))

Dilate pore space:

Use spherical structuring element of radius r

B = dilate (1 - B, sphere(r))

Mask with original pore space:

B = B AND (1 - A)

Calculate current pressure:

$P = 2 \times \sigma \times \cos(\theta) / (r \times Res)$

Check for connectivity:

Set the first slice of B to 1

L = label connected components in B

B = region in L connected to the first slice

Check for breakthroughs:

If any pixel in the last slice of B is 1:

LEP = P

Exit loop

Return LEP

The algorithm begins by initializing the membrane structure A and calculating its distance transform D (which is explained in the next paragraph), which provides information about maximal pore sizes (r_{max}) and helps to set the beginning of the simulation loop assuming a very low water pressure and a large curvature radius. The spatial resolution (Res), contact angle (θ), and interfacial tension (σ) are set based on the specific membrane and fluid properties.

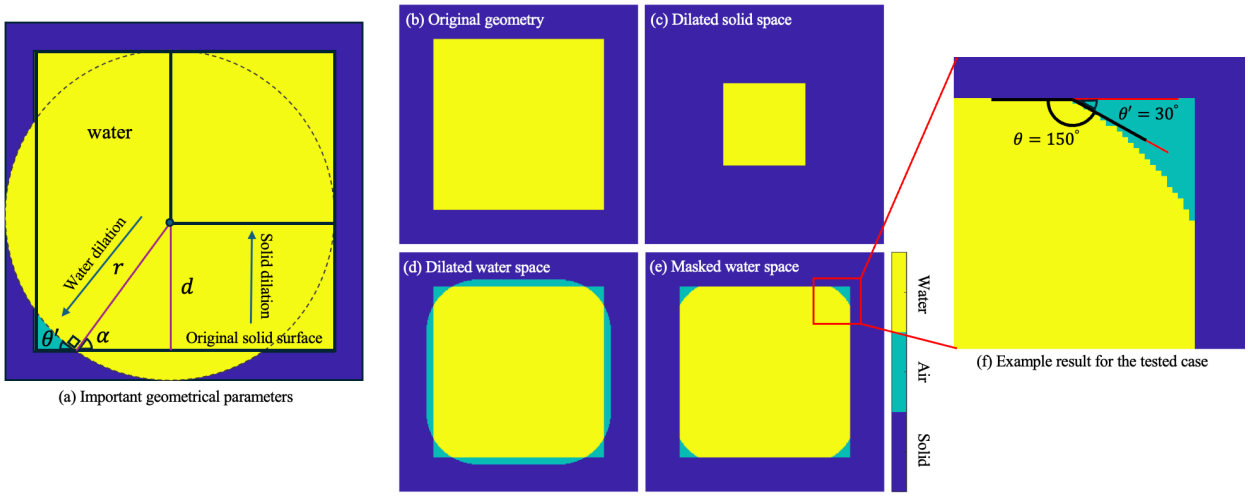

Fig. 3-3. (a) Geometrical parameters including r, d, θ, θ', and α; example results of the algorithm for a 2D square pore: (b) Original geometry, (c) Dilated solid space, (d) Dilated water space, (e) Masked water space, and (f) Example result for the tested case.

The bwdist function (distance transform) computes the Euclidean distance from each pixel to the nearest non-zero pixel in the binary image (Fig. 3-4) [27].

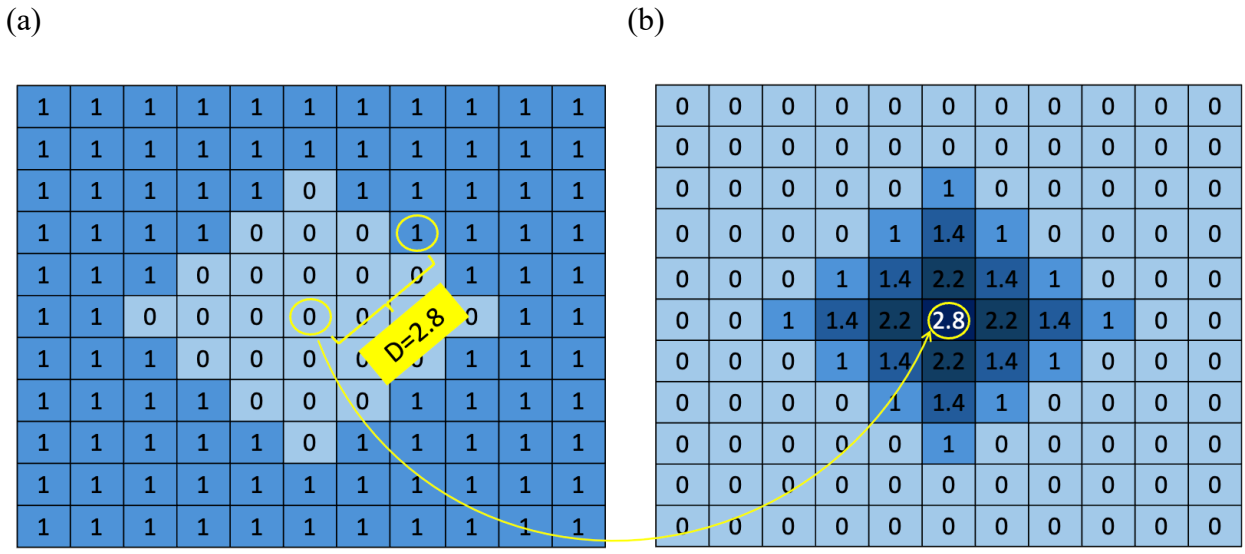

Fig. 3-4. Distance transform definition in a matrix: (a) a 2D binary image, and (b) the corresponding Euclidean distance from each pixel to the closest non-zero pixel.

The main loop iterates through decreasing radii of curvature, effectively simulating increasing pressure. For each iteration, the algorithm simulates the invasion of the non-wetting fluid (water in this case) into the porous structure using a series of morphological operations.

First, the solid phase is dilated by a distance $d = r \times \cos(\theta)$, where r is the current radius of curvature (Fig. 3-3c). The dilation is performed using a spherical structuring element to maintain the curvature of the interface.

Next, the resulting pore space is dilated by the radius of curvature r, simulating the invasion of the non-wetting fluid (Fig. 3-3d). Again, a spherical structuring element is used to maintain the appropriate curvature. This dilation creates space for the fluid interface to satisfy the contact angle condition. The resulting fluid distribution is then masked with the original pore space to ensure the fluid remains within the porous structure (Fig. 3-3e). Fig. 3-3f provides a close-up example of the

result for a contact angle of 30 degrees and an interface radius of 60 pixels, applied to the image of a square pore with 200×200 pixels.

In other words, when a shape gets eroded, and then dilated, this shape forgets that it had sharp edges (Fig. 3-5).

a) Eroding the geometry:

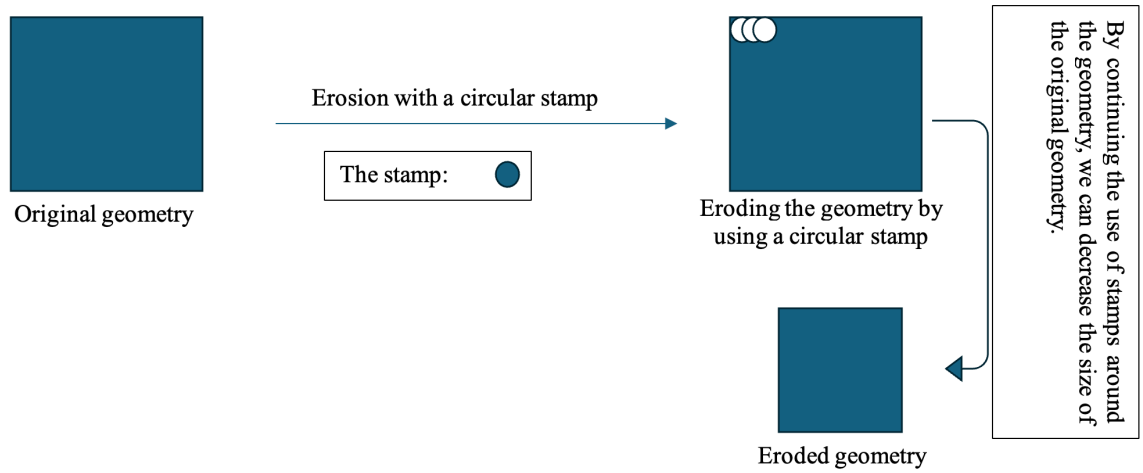

b) Dilating the geometry:

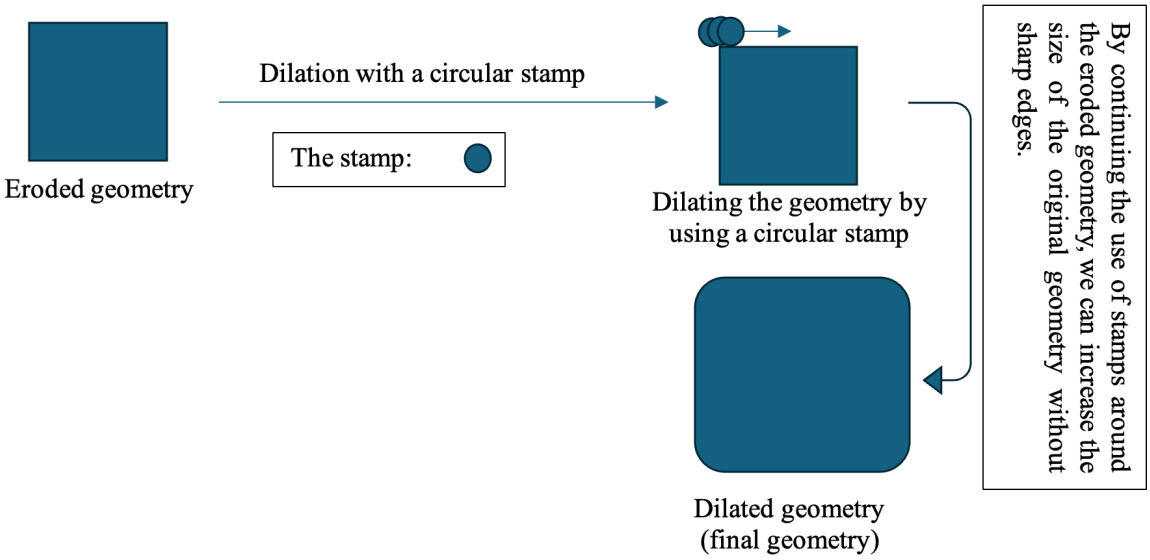

Fig. 3-5. The process of edge removal and applying the effect of contact angle through two consecutive morphological operations: a) Eroding the geometry, and b) Dilating the geometry.

After each iteration, a connectivity check determines if the invading fluid is connected to the inlet face. This is done by labeling connected components and excluding any component that has a label different from the inlet face. This step ensures that only connected fluid paths are considered, eliminating isolated fluid regions. Then at the end of each iteration, the outlet face of the geometry is checked to see if water is present which is the indication of fluid breakthrough. When the breakthrough occurs, the current pressure is recorded as the LEP, and the algorithm terminates; the flow chart of the process can be seen in Fig 3-6.

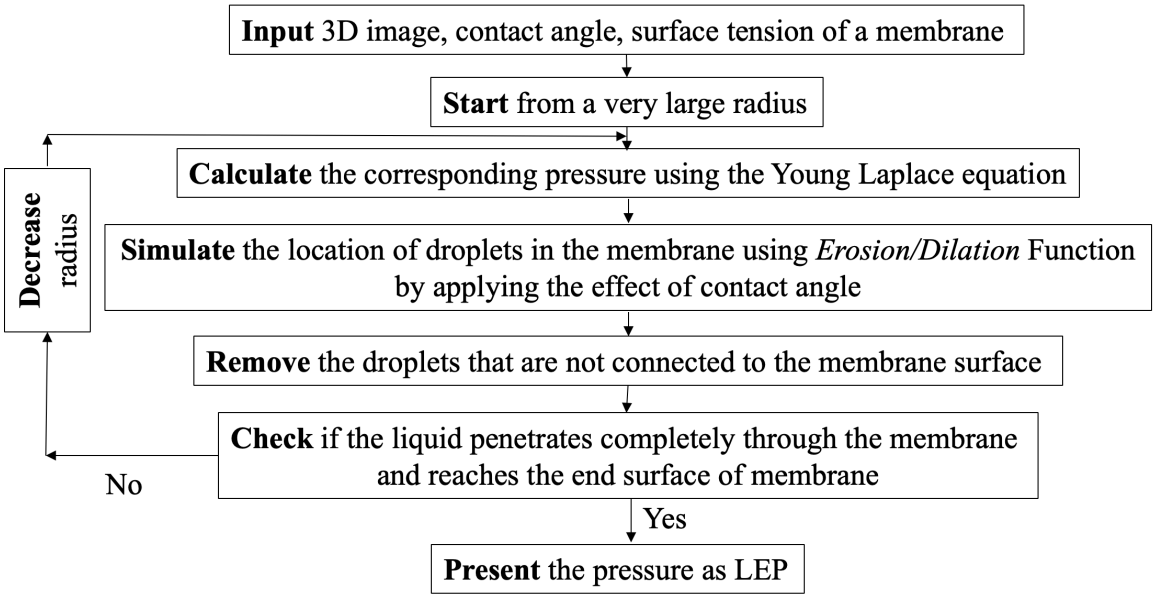

Fig. 3-6. The flow chart of the LEP estimation process in this work.

Fig. 3-7 illustrates the process of pore wetting during LEP measurement for a randomly generated structure, developed using our model.

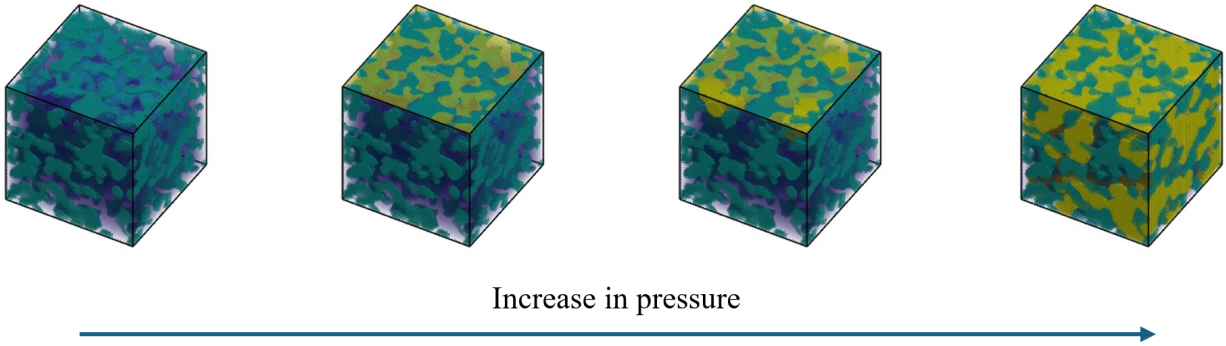

Fig. 3-7. Process of pore wetting in a random structure with the size of 100×100×100 pixels in which yellow represents water.

It is noteworthy to mention that the process of LEP estimation is very quick and is done only in several minutes; the computation time depends on the image size (as can be seen in Fig. 3-8).

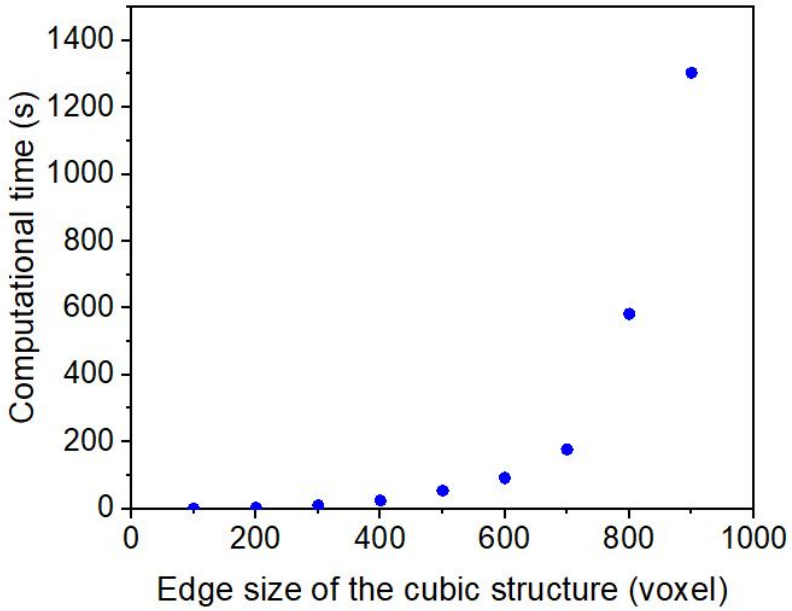

Fig. 3-8. LEP estimation computational time for cubic structures with different edge sizes (for example for a 100 ×100 ×100 structure, the computational time is only 0.73s).

3.4.2. Model validation

For the mentioned membrane in section 3.3.1 Materials, PT20, segmented 3D images, with a pixel size of 38.99 nm, provided by [25], were used for model validation. The reported LEP for the PT20 membrane based on [27] was 3.68 Bar and the contact angle for this membrane based on [24] was 140°. Surface tension was considered to be 7.2×10^{-2} N/m at 25 °C between water and air. In this work, the developed model estimated the LEP for a 200×200×1750 pixels structure of the PT20 membrane, and it was 3.81 Bar. The reason for choosing a part of the 3D image instead of the whole sample (200×200×1750 out of 927×927×1926) was that the image consisted of imperfect parts which did not show the pores properly, therefore, only the intact part of the image was used.

3.4.3. Effect of membrane properties on LEP

In this section, the effects of membrane properties such as maximum pore radius, mean pore radius, and mean throat radius on LEP are studied. For this purpose, two hundred random structures were generated in a MATLAB environment and then the mentioned parameters were calculated for each of these structures. Random 3D membrane structures were generated with the same porosity through random initialization, Gaussian smoothing, and thresholding. Initially, a 100×100×100 matrix filled with uniformly distributed random values, between 0 and 1, is created. This matrix is then smoothed using a 3D Gaussian filter with a specified standard deviation, which blurs the values to form continuous regions. The quantile function calculates a threshold value based on the desired porosity, ensuring that a certain fraction of the matrix values is below this threshold. Finally, the matrix is binarized by setting elements greater than the threshold value to 1 (representing solid material) and the rest to 0 (representing pores), thus forming a random 3D structure with controlled porosity as can be seen in Fig. 3-9.

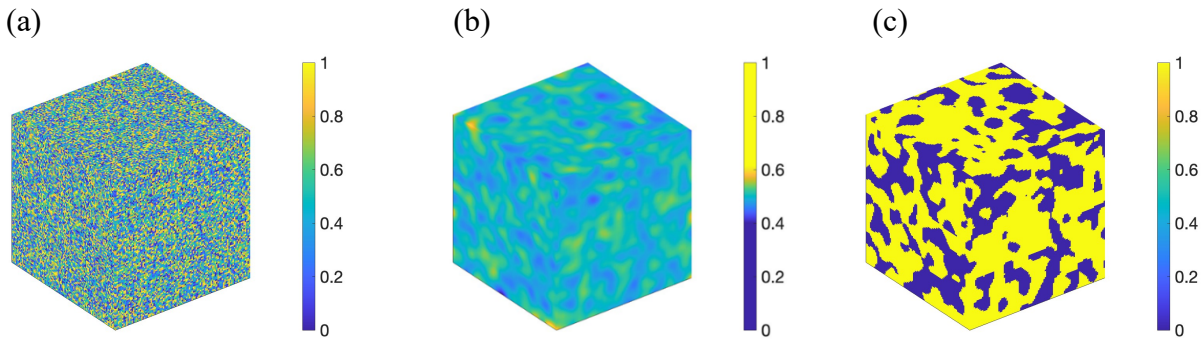

Fig. 3-9. Process of generating random 3D membrane structures: (a) random initialization: A 100×100×100 matrix filled with uniformly distributed random values between 0 and 1; (b) Gaussian smoothing: the matrix is smoothed using a 3D Gaussian filter, creating continuous regions; (c) thresholding: the smoothed matrix is binarized using a threshold, forming a structure with solid material (yellow) and pores (blue).

We developed some models to estimate the mentioned parameters, i.e., maximum pore radius, mean pore radius, and mean throat radius, in MATLAB environment. In these codes, the membrane is presented as a binary matrix in which 1 represents the solid phase and 0 represents the pore phase.

In the code, pores and throats are detected using a combination of image processing techniques, particularly Euclidean distance transform and watershed segmentation algorithm. First, the Euclidean distance transform is applied to calculate the distance of each point in the pore space from the nearest solid boundary. This distance map helps in identifying the boundaries between connected pores. Next, the watershed segmentation technique uses the distance information to detect the narrowest points between connected pores, which are defined as the throats. The regions surrounded by throats are classified as pores. The concept is based on topography; imagine the surface of the porous material like a landscape with valleys and hills, where pores are represented as valleys and throats as the narrow connections between them. As "water" rises in the valleys, it encounters a ridge, which is marked as the throat. By cutting along these ridges, the watershed

method effectively separates pores and throats [28, 29]. To measure pore size, each pore is characterized based on the volume and shape of the segmented regions; the segmented images are analyzed, and each identified pore is approximated to a spherical shape, with the diameter of the sphere equal to the diameter of the real pore. The throat size is measured by evaluating the cross-sectional area at the narrowest point of the connection between two adjacent pores [29]. Therefore, the maximum pore radius, the average pore radius, and the average throat radius can be found. Figs. 3-10a, 3-10b, and 3-10c show the effects of maximum pore radius, mean pore radius, and mean throat radius on LEP, respectively. As the maximum pore radius and mean pore radius increase, the LEP decreases, as shown in Figs. 3-10a and 3-10b. With a larger pore radius, the denominator in the Laplace equation increases, resulting in a lower LEP. This finding is expected and aligns with the literature [16]. However, the advantage of this approach is that it considers only the large pores connected to the surface, excluding isolated pores from the model, which may otherwise cause false LEP values. As shown in Fig. 3-10c, the increase in mean throat radius decreases LEP.

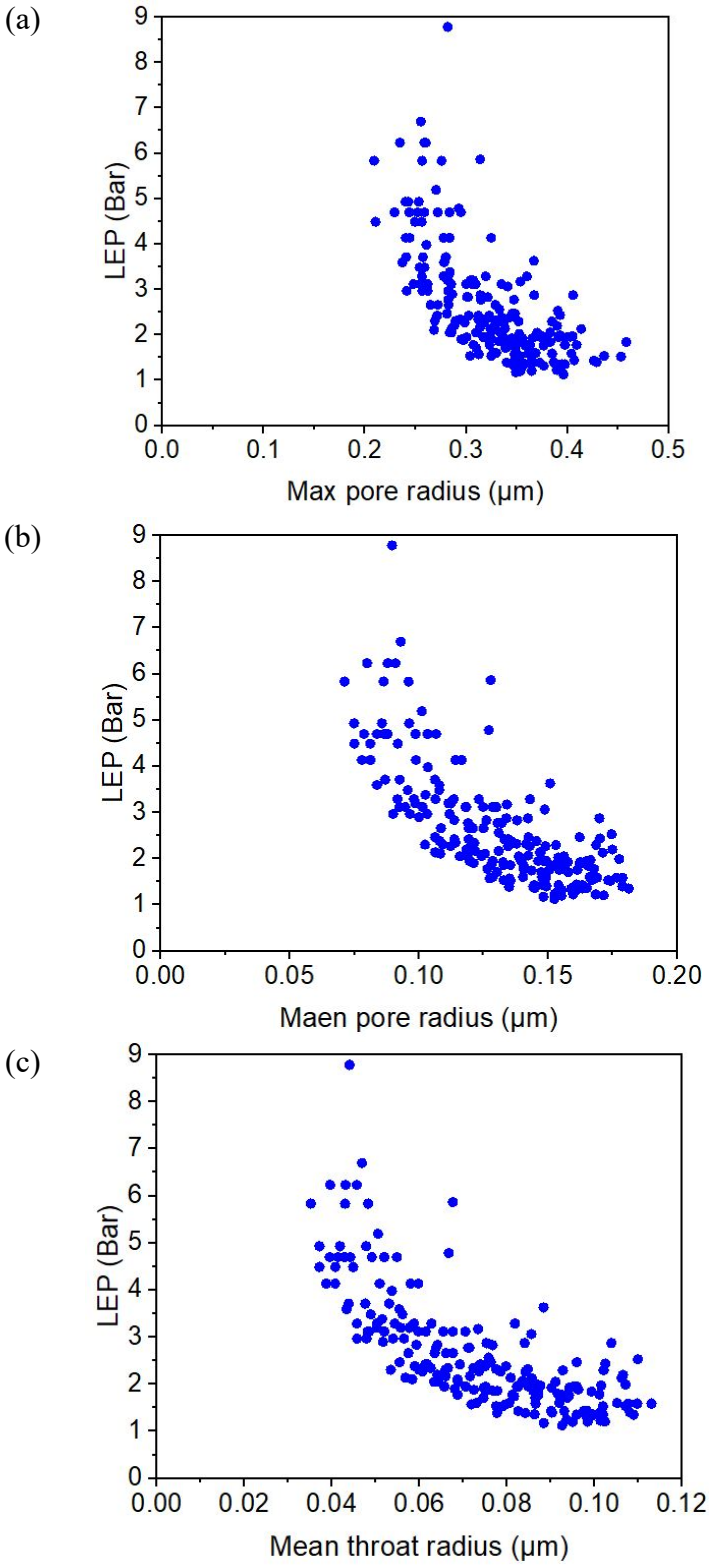

Fig. 3-10. The influence of (a) max pore radius, (b) mean pore radius, and (c) mean throat radius, on LEP for 200 random structures with a contact angle of 150˚.

3.5. Conclusions

In this study, a model capable of estimating LEP was developed. Using the 3D image of a membrane, the model calculates LEP very quickly, within a few minutes, in contrast to CFD modeling, which may take days to simulate water flows through the micro-scale porous structure. Additionally, unlike most previous models used for LEP estimation, which assume pores are ideal tori or cylinders, the newly developed model considers the actual structure of the membrane, resulting in more accurate LEP estimation. The model was validated using experimental LEP data for the PT20 membrane, obtained from previously published works, with achieving less than a 5 percent error. Furthermore, custom-built codes were developed to estimate the maximum pore radius, mean pore radius, and mean throat radius. Two hundred random synthetic membrane structures were generated, and for each structure, the maximum pore radius, mean pore radius, mean throat radius, and LEP were calculated for water at 25˚C with a contact angle of 150˚, and consequently the effects of the mentioned parameters on LEP were evaluated. Finally, this 3D morphology-based model in addition to estimating LEP rapidly, can be useful in term of helping to design optimized structures for future works.

3.6. References

[1] Pedro-Monzonís M, Solera A, Ferrer J, Estrela T, Paredes-Arquiola J. A review of water scarcity and drought indexes in water resources planning and management. J Hydrol (Amst) 2015;527:482–93. https://doi.org/10.1016/j.jhydrol.2015.05.003.

[2] Khondoker M, Mandal S, Gurav R, Hwang S. Freshwater shortage, salinity increase, and global food production: A need for sustainable irrigation water desalination - A scoping review. Earth 2023;4:223–40. https://doi.org/10.3390/earth4020012.

[3] Zeng Z, Liu J, Savenije HHG. A simple approach to assess water scarcity integrating water quantity and quality. Ecol Indic 2013;34:441–9. https://doi.org/10.1016/j.ecolind.2013.06.012.

[4] Mishra RK. Fresh water availability and its global challenge. British Journal of Multidisciplinary and Advanced Studies 2023;4:1–78. https://doi.org/10.37745/bjmas.2022.0208.

[5] Baghbanzadeh M, Rana D, Lan CQ, Matsuura T. Zero thermal input membrane distillation, a zero-waste and sustainable solution for freshwater shortage. Appl Energy 2017;187:910–28. https://doi.org/10.1016/j.apenergy.2016.10.142.

[6] Ren F, Yang G, Li W, He X, Gao Y, Tian L, et al. Yield-compatible salinity level for growing cotton (*Gossypium hirsutum* L.) under mulched drip irrigation using saline water. Agric Water Manag 2021;250:106859. https://doi.org/10.1016/j.agwat.2021.106859.

[7] Curto D, Franzitta V, Guercio A. A review of the water desalination technologies. Applied Sciences 2021;11:670. https://doi.org/10.3390/app11020670.

[8] Chen X, Boo C, Yip NY. Transport and structural properties of osmotic membranes in high-salinity desalination using cascading osmotically mediated reverse osmosis. Desalination 2020;479:114335. https://doi.org/10.1016/j.desal.2020.114335.

[9] Greenlee LF, Lawler DF, Freeman BD, Marrot B, Moulin P. Reverse osmosis desalination: Water sources, technology, and today's challenges. Water Res 2009;43:2317–48. https://doi.org/10.1016/j.watres.2009.03.010.

[10] Davenport DM, Ritt CL, Verbeke R, Dickmann M, Egger W, Vankelecom IFJ, et al. Thin film composite membrane compaction in high-pressure reverse osmosis. J Memb Sci 2020;610:118268. https://doi.org/10.1016/j.memsci.2020.118268.

[11] Khraisheh M, Dawas N, Nasser MS, Al-Marri MJ, Hussien MA, Adham S, et al. Osmotic pressure estimation using the Pitzer equation for forward osmosis modelling. Environ Technol 2020;41:2533–45. https://doi.org/10.1080/09593330.2019.1575476.

[12] Alkhudhiri A, Darwish N, Hilal N. Membrane distillation: A comprehensive review. Desalination 2012;287:2–18. https://doi.org/10.1016/j.desal.2011.08.027.

[13] Swaminathan J, Chung HW, Warsinger DM, Lienhard V JH. Energy efficiency of membrane distillation up to high salinity: Evaluating critical system size and optimal membrane thickness. Appl Energy 2018;211:715–34. https://doi.org/10.1016/j.apenergy.2017.11.043.

[14] Chamani H, Woloszyn J, Matsuura T, Rana D, Lan CQ. Pore wetting in membrane distillation: A comprehensive review. Prog Mater Sci 2021;122:100843. https://doi.org/10.1016/j.pmatsci.2021.100843.

[15] Guillen-Burrieza E, Servi A, Lalia BS, Arafat HA. Membrane structure and surface morphology impact on the wetting of MD membranes. J Memb Sci 2015;483:94–103. https://doi.org/10.1016/j.memsci.2015.02.024.

[16] Chamani H, Yazgan-Birgi P, Matsuura T, Rana D, Hassan Ali MI, Arafat HA, et al. CFD-based genetic programming model for liquid entry pressure estimation of hydrophobic membranes. Desalination 2020;476:114231. https://doi.org/10.1016/j.desal.2019.114231.

[17] Franken ACM, Nolten JAM, Mulder MHV, Bargeman D, Smolders CA. Wetting criteria for the applicability of membrane distillation. J Memb Sci 1987;33:315–28. https://doi.org/10.1016/S0376-7388(00)80288-4.

[18] Kim B-S, Harriott P. Critical entry pressure for liquids in hydrophobic membranes. J Colloid Interface Sci 1987;115:1–8. https://doi.org/10.1016/0021-9797(87)90002-6.

[19] Servi AT, Kharraz J, Klee D, Notarangelo K, Eyob B, Guillen-Burrieza E, et al. A systematic study of the impact of hydrophobicity on the wetting of MD membranes. J Memb Sci 2016;520:850–9. https://doi.org/10.1016/j.memsci.2016.08.021.

[20] Yazgan-Birgi P, Hassan Ali MI, Arafat HA. Estimation of liquid entry pressure in hydrophobic membranes using CFD tools. J Memb Sci 2018;552:68–76. https://doi.org/10.1016/j.memsci.2018.01.061.

[21] Jäger T, Mokos A, Prasianakis NI, Leyer S. Pore-level multiphase simulations of realistic distillation membranes for water desalination. Membranes (Basel) 2022;12:1112. https://doi.org/10.3390/membranes12111112.

[22] Hilpert M, Miller CT. Pore-morphology-based simulation of drainage in totally wetting porous media. Adv Water Resour 2001;24:243–55. https://doi.org/10.1016/S0309-1708(00)00056-7.

[23] Rácz G, Kerker S, Kovács Z, Vatai G, Ebrahimi M, Czermak P. Theoretical and experimental approaches of liquid entry pressure determination in membrane distillation processes. Periodica Polytechnica Chemical Engineering 2014;58:81–91. https://doi.org/10.3311/PPch.2179.

[24] Cramer K, Prasianakis NI, Niceno B, Ihli J, Holler M, Leyer S. Three-dimensional membrane imaging with X-ray ptychography: Determination of membrane transport properties for membrane distillation. Transp Porous Media 2021;138:265–84. https://doi.org/10.1007/s11242-021-01603-4.

[25] Holzer L, Marmet P, Fingerle M, Wiegmann A, Neumann M, Schmidt V. Tortuosity-porosity relationships: Review of empirical data from literature. In: Tortuosity and Microstructure Effects in Porous Media. Springer Series in Materials Science, vol. 333, Springer, Cham, 2023, Ch. 3, p. 51–89. https://doi.org/10.1007/978-3-031-30477-4_3.

[26] Agrawal P, Mascini A, Bultreys T, Aslannejad H, Wolthers M, Cnudde V, et al. The impact of pore-throat shape evolution during dissolution on carbonate rock permeability: Pore network modeling and experiments. Adv Water Resour 2021;155:103991. https://doi.org/10.1016/j.advwatres.2021.103991.

[27] Izquierdo-Gil MA, García-Payo MC, Fernández-Pineda C. Air gap membrane distillation of sucrose aqueous solutions. J Memb Sci 1999;155:291–307. https://doi.org/10.1016/S0376-7388(98)00323-8.

[28] Durham RJ, Nguyen MH. Hydrophobic membrane evaluation and cleaning for osmotic distillation of tomato puree. J Memb Sci 1994;87:181–9. https://doi.org/10.1016/0376-7388(93)E0142-7.

[29] Rabbani A, Jamshidi S, Salehi S. An automated simple algorithm for realistic pore network extraction from micro-tomography images. J Pet Sci Eng 2014;123:164–71. https://doi.org/10.1016/j.petrol.2014.08.020.

[30] Rabbani A, Babaei M. Hybrid pore-network and lattice-Boltzmann permeability modelling accelerated by machine learning. Adv Water Resour 2019;126:116–28. https://doi.org/10.1016/j.advwatres.2019.02.012.

[31] Al-Raoush RI, Madhoun IT. TORT3D: A MATLAB code to compute geometric tortuosity from 3D images of unconsolidated porous media. Powder Technol 2017; 320:99–107. https://doi.org/10.1016/j.powtec.2017.06.066.

Chapter 4: Conclusions and future works

Recently, water scarcity has become a global issue due to the increase in population and climate change. Although most of the Earth's surface is water, only 3% of these water resources are fresh water, and just 0.06% of that is easily accessible. Therefore, it is really important to focus on desalination processes. Membrane desalination is one of the most important processes for desalination. Membrane Distillation (MD) can be a solution to desalt high salinity brines, but commercialization of this process has not happened yet mainly due to the pore wetting. When instead of vapour, liquid passes through the pores of a hydrophobic membrane in MD process, pore wetting happens which reduces the effectiveness of the process.

Hydrophobicity plays an important role in all membrane-based processes, as it indicates the behavior of liquid (water) on the surface of the membrane. Janus membranes have drawn attention recently because of their ability to direct the water flow in a controlled manner, as they can have two sides with different hydrophobicity.

In this thesis, we have studied hydrophobicity and wetting resistance from two different lenses.

In the first study, *modeling of water transport in Janus membrane*, a theoretical model was developed to explain the transport of fluid within Janus membranes that have asymmetric properties with hydrophilic and hydrophobic sides. Previous models could not fully explain the fluid transport without considering the complex re-entrant structures, which was the enlarging of the water channel width toward the bottom of the membrane. By using the Young equation, a simpler model was developed in this study, considering the surface energy change that is caused by the movement of water from hydrophilic to hydrophobic sides in a cylindrical pore. The model accounts for important factors, including the critical pressure required for directional water flow and the improved flux when a hydrophobic layer is applied to a hydrophilic substrate.

Furthermore, this model also presents surface energy as a driving force for water transport, rather than traditional reliance on capillary forces. This novel perspective helps to understand the transport behaviour in Janus membranes and also provides a simple approach for critical pressure calculation and membrane performance assessment. Therefore, by using this model we can easily calculate the required pressure, critical pressure, to have water flow when we have hydrophilic/hydrophobic configuration without requiring the presence of water/air interface in the pore and re-entrant structure, and also, we can calculate the flow rate within the pores of the Janus membranes for the first time.

Importantly, the prediction of a hysteresis loop in the pressure-flow curve of these membranes could lead to the development of more efficient membranes with enhanced directional transport capabilities. Additionally, the model shows that we can prevent pore wetting in MD by using a hydrophilic/hydrophobic configuration in the hydrophobic layer as the critical pressure of this configuration more than doubles LEP of corresponding hydrophobic layer.

In the second study, *3D morphology-based analysis for liquid entry pressure (LEP) estimation*, a 3D morphology-based model was developed for estimating LEP which is a critical parameter in hydrophobic membranes to evaluate the wetting resistance of membranes in MD. Unlike the traditional models that assumed ideal pore structures, such as cylindrical pores, which do not accurately represent the complex geometry of real membranes, this study considers the real structure of membranes by using 3D images of the membrane structure. This approach helps to estimate the LEP rapidly and accurately. By doing so, the model significantly improves the speed of LEP estimation compared to conventional computational fluid dynamics (CFD) simulations, which are typically time-consuming and computationally intensive at pore scale.

The model was validated by using a commercial membrane, PT20 membrane, and the reported LEP value in a previously published literature; there was less than 5% error in LEP prediction, which shows the model's reliability. Moreover, the development of custom-built codes to estimate key membrane properties, such as pore radius, and throat radius, provides a comprehensive tool for analyzing the membrane structure; the model can help provide a better understanding of the effects of different morphological characteristics on LEP and thereby facilitating membrane development. This advancement in LEP estimation is especially important for MD applications, where preventing pore wetting is critical to maintain membrane performance and ensure the purity of the permeate.

Although the models presented in this thesis provide valuable insights, they still suffer from some limitations which can be tackled in future work. For instance, the Janus membrane model assumes ideal transitions between hydrophilic and hydrophobic surfaces, which may not fully represent the behaviour of more complex or heterogeneous membranes in practical applications. Also, an ideal shape was studied; in future works, a 3D morphology-based model, inspired by the work in Chapter 3, can be employed to analyze the transport within the Janus membranes based on the real shape of the membrane.

There are some limitations in LEP estimation regarding the use of 3D images such as image resolution constraints. Moreover, the LEP estimation model could be validated with more experiments to enhance its reliability. In this study, a model for LEP estimation was introduced; in future work, another model can be developed to estimate the flux. Again, the existing models for fluid flow within the membrane pore, such as the Hagen-Poiseuille equation, and Washburn's equation, oversimplify the intricate interconnected nature of actual membrane structures by

assuming uniform separate cylindrical pores when modeling permeability, and it is suggested to develop a model which can estimate permeability using 3D images of the membranes quickly.

Then, a user-friendly open-source tool can be developed for estimating LEP and permeability, which receives the 3D image of the membrane, membrane contact angle, and pixel size of the 3D image and estimates LEP and permeability.

An appropriate membrane for MD should have both high wetting resistance, or in other words LEP, and high flux. With tools for estimating LEP and flux, an optimization algorithm, probably Bayesian optimization, can be developed to modify and design the membrane structures to achieve both high LEP and flux by optimizing properties of the 3D structure of the membrane, such as pore shape, pore density, connectivity, tortuosity, and pore size distribution. Optimizing 3D structures will help membrane scientists develop more optimal structures. Also, advancements in 3D printing resolution and materials will eventually allow them to fabricate custom-designed membranes, reducing the trial-and-error process in laboratories.

In conclusion, this thesis helps to have a better understanding of water transport within the Janus membrane and also presents a new approach to estimating LEP for MD membranes.